Maximizing the accuracy of finite element simulation of elastic wave propagation in polycrystals

M. Huang[1,a], G. Sha[2], P. Huthwaite[1], S. I. Rokhlin[2], and M. J. S. Lowe[1]

[1]Department of Mechanical Engineering,

Imperial College London,

Exhibition Road, London SW7 2AZ, United Kingdom

[2]Department of Materials Science and Engineering,

Edison Joining Technology Center,

The Ohio State University,

1248 Arthur E. Adams Drive Columbus, Ohio 43221, United States

[a] Electronic mail: m.huang16@imperial.ac.uk

Manuscript accepted for publication in J. Acoust. Soc. Am. 148 (4), October 2020.

ABSTRACT

Three-dimensional finite element (FE) modelling, with representation of materials at grain scale in realistic sample volumes, is capable of accurately describing elastic wave propagation and scattering within polycrystals. A broader and better future use of this FE method requires several important topics to be fully understood, and this work presents studies addressing this aim. The first topic concerns the determination of effective media parameters, namely scattering induced attenuation and phase velocity, from measured coherent waves. This work evaluates two determination approaches, through-transmission and fitting, and it is found that they are practically equivalent and can thus be used interchangeably. For the second topic of estimating modelling errors and uncertainties, this work performs thorough analytical and numerical studies to estimate those caused by both FE approximations and statistical considerations. It is demonstrated that the errors and uncertainties can be well suppressed by using a proper combination of modelling parameters. For the last topic of incorporating FE model information into theoretical models, this work presents elaborated investigations and shows that to improve agreement between the FE and theoretical models the symmetry boundary conditions used in FE models need to be considered in the two-point correlation function, which is required by theoretical models.

Keywords: elastic wave; finite element; polycrystal; attenuation and phase velocity; error and uncertainty; two-point correlation

I. INTRODUCTION

A polycrystalline material is composed of elastically anisotropic grains with differently oriented crystallographic axes. The elastic properties within such a medium are thus spatially varied, and elastic waves are scattered as they propagate, leading to the waves being attenuated and their phase velocities being dispersive. These wave behaviors are undesirable to the non-destructive testing for the detection of defects, a major reason of which is that attenuation can weaken the detected signal that may be masked by the grain scattering noise [1]. On the other hand, the wave behaviors can also be used advantageously for the characterization of microstructure because both attenuation and dispersion carry bulk information about grain structures[2,3]. Therefore, understanding these behaviors is practically important.

Extensive researches have been carried out to understand the behaviors of elastic waves in polycrystals. Early works, a review of which can be found in Papadakis[4], focused on experimental investigations and the theoretical explanations of experimental results. These early efforts led to a variety of theoretical models that showed good qualitative agreement with experiments[4], but each of them is applicable only to a specific scattering regime. A unified model that is valid across all scattering regimes was first presented by Stanke and Kino[5] by applying the Keller approximation[6,7] to polycrystalline media. An equivalent model was later developed by Weaver[8] based on the Dyson equation with the introduction of the first-order smoothing approximation[9]. Further theoretical developments[2,10,19,11–18] were mostly extensions of these two models, the Weaver model in particular due to its ease of extension, to various polycrystals of different elastic properties and grain geometries.

Theoretical models are necessarily approximate, because it is impossible to carry a rigorous

mathematical description through all steps of the model development. Therefore, assumptions and approximations are made in the derivations, leading to expected, but mostly not quantified, approximations in the outputs. The Stanke and Kino[5] and Weaver[8] models are accurate up to the second order of material inhomogeneities, offering them possibilities of considering forward multiple scattering. However, except the rare cases[13,16–20] that maintained the second-order accuracy, other developments[2,10–12,14,15] of the Weaver model (including the eventual formulation of Weaver[8]) were formulated by invoking the Born approximation to facilitate explicit calculations for attenuation. Such treatment limits the validities of the models to even lower-order scattering in frequency ranges below the geometric regime[8].

In contrast to theoretical studies, numerical simulations can be performed without the approximations of low order scattering. A wide range of numerical methods can be employed to achieve such numerical experiments and a summary of them can be found in Van Pamel et al.[21]. Among these methods, the finite element (FE) method is widely researched for the simulation of elastic waves in complex media[22]. The use of this method for polycrystals has long been limited, by its extreme computational demands, to two-dimensional (2D) cases[23–28]. However, the dependence of scattering on spatial dimensionality[29] at certain frequencies means that 3D simulation is always desirable for understanding real-world wave phenomena. Recent advancements of computer hardware and elastodynamic software, especially the development of the GPU-accelerated Pogo program[30], have enabled the successes of 3D modelling[18,19,21,31,32]. These 3D simulation studies, with representations of polycrystals at grain scale in realistic sample volumes, addressed a relatively simple case of plane longitudinal waves propagating in polycrystals with macroscopically isotropic elastic properties and equiaxed grains. They have demonstrated that 3D FE simulations can accurately describe the interactions of

elastic waves with grains that involve complex multiple scattering.

Due to the flexibility and accuracy of 3D FE modelling, we can expect that there will be a surge of modelling studies in the future to understand and optimize practical inspection problems, and to evaluate the approximations of theoretical models for model-based applications, such as the inverse characterization of microstructure. However, even for the relatively simple cases addressed so far[18,19,21,31,32], some essential topics are not yet understood well enough to allow confidence that the best accuracy of simulation is being achieved. The authors have been investigating this challenge, and the purpose of this article is to report on important topics of modelling methodology for which new knowledge will inform a reliable quality of simulation performance.

The first topic is the determination of effective media parameters from the simulation results, namely attenuation and phase velocity. An important task of these addressed to 3D FE simulations is to understand how a transmitted plane wave changes with propagation distance. This change is parametrically described by attenuation coefficient and phase velocity, representing respectively the amplitude and phase parts of the change. One can perform the determination in a through-transmission configuration, which is commonly used in actual experiments where access is limited to sample surfaces. This method has seen wide applications in our previous simulations[18,19,21,29,31], in which the effective media parameters are determined by comparing the two waves measured on the transmitting surface and its opposite receiving surface. Alternatively, one can also determine the parameters by best fitting the waves acquired on multiple surfaces within the simulation volume that are parallel to the transmitting surface. This fitting method was first used in a recent work[32] and it is made possible by the intrinsic advantage of FE modelling that waves inside a sample can be easily measured. Each of these two methods has

its own advantages: the through-transmission method is consistent with physical experimental configurations, so it is conceptually attractive, and it requires relatively little measured data, while the fitting method can potentially provide more abundant information about wave-microstructure interaction. However, these two methods have not been compared in actual simulations to identify their ranges of application and their possible advantages and drawbacks. It is important to recognize that while the difference between these methods would be trivial for a homogeneous material, this is not the case for a polycrystal: the grain scattering creates high levels of noise in the measurements of the coherent signals as well as local influences of multiple scattering, both of which bring significant uncertainty to the measurements.

The second topic concerns the errors and uncertainties of the determined scattering parameters. It is known that numerical approximations, including the space and time discretization in the FE method and the inexactness in finite-precision computations, can cause numerical errors. In addition, statistical considerations, involving the random distribution of grain structures and the stochastic pattern of wave scattering, can induce both statistical errors and uncertainties. For numerical errors, studies so far were partly limited to homogeneous and isotropic materials[33,34] and were partly qualitative when they went to polycrystalline materials[21,31]; while for statistical errors and uncertainties, attention has not yet been turned to the specific problem of wave propagation within polycrystals.

The third of our three topics of study involves the evaluation of the performance of theoretical models using the simulation data of 3D FE modelling. The simulations are ideal for the evaluation of the effects of the approximations of theoretical models, as they can be fully controlled, and their errors and uncertainties can to some extent be estimated. The evaluation requires the statistical information of FE material systems being measured and being put into theoretical models. Such

information is represented by the two-point correlation (TPC) function for widely used theoretical models, like the second-order[5,8,18,19] and far-field[20] approximations. Previous studies[18,19,32] have been successful in incorporating the TPC function of polycrystal models into theoretical models, and have shown good agreement between FE and theoretical results in terms of scattering parameters. However, these studies neglected in their TPC functions the fact that symmetry boundary conditions, employed to emulate infinitely wide media that can hold plane waves, actually mirror the boundary grains of FE models and thus make the grains doubled in volume.

For the benefit of future applications of the 3D FE method, this work presents a thorough discussion of the above-mentioned topics, with the aim to solve them appropriately. The discussion focuses on the same simulation case addressed in currently-available works[18,19,21,31,32], which is the propagation of plane longitudinal waves in polycrystals with untextured properties and equiaxed grains. The goal of this work, however, is to lay a solid foundation for general cases of arbitrary wave modalities in any polycrystalline material system. For the specific case concerned in this work, its 3D FE model is summarized in Sec. II. The subsequent three sections discuss respectively the three topics mentioned above. Sec. III deals with the determination of effective media parameters. Sec. IV presents a systematic study of errors and uncertainties, with discussions on how to suppress them. Sec. V provides a comprehensive discussion covering the incorporation of 3D FE simulation data into theoretical models and the proper consideration of SBCs in this incorporation procedure.

II. FINITE ELEMENT METHOD FOR ELASTIC WAVES IN POLYCRYSTALS

The three studies reported here were conducted using a three-dimensional finite element (FE) model of a volume of a polycrystal, simulating the propagation of plane longitudinal waves in the time domain. This kind of model and studies using it have been reported previously[21,31,32], but for the convenience of subsequent discussions, we provide in the following a summary of the method.

A. Representation of polycrystals at grain scale

Scattering only occurs when grains are present, so the representation of polycrystals at grain scale is the key to reproduce scattering. Researchers have simulated the spatial properties of polycrystals with several methods, two popular ones being Voronoi tessellation (e.g. Quey et al.[35]) and Dream.3D[36]. In this work we have used Voronoi tessellation[35].

The Voronoi tessellation partitions a cuboid model, which is shown in Fig. 1, into convex polyhedra or grains that have no overlaps and no gaps. Each grain encloses a seed that is specified beforehand and all points in this grain are closer to its own seed than to any other. Grain statistics, like grain size distribution and average grain shape, are determined by how the seeds are specified. The present work uses a relatively simple seeding procedure which utilizes a Poisson point process to drop random seeds into the model space. As would be expected from the central limit theorem, the grain sizes (specifically the cubic roots of grain volumes) of the generated model are normally distributed[21] and the grain shapes are equiaxed on average. For later discussions, three such models are generated, and their parameters are provided in Table I.

Material properties are then assigned to the generated models. This study considers single-phase polycrystals, and therefore the grains of each model belong to the same crystal material. The two materials considered in this study are given in Table II, both having cubic symmetry and being

chosen as examples of weakly and strongly scattering materials, respectively. Although in each model all grains share an identical material, their crystallographic axes are randomly oriented. Therefore, the models are homogeneous and statically isotropic on the macroscopic scale.

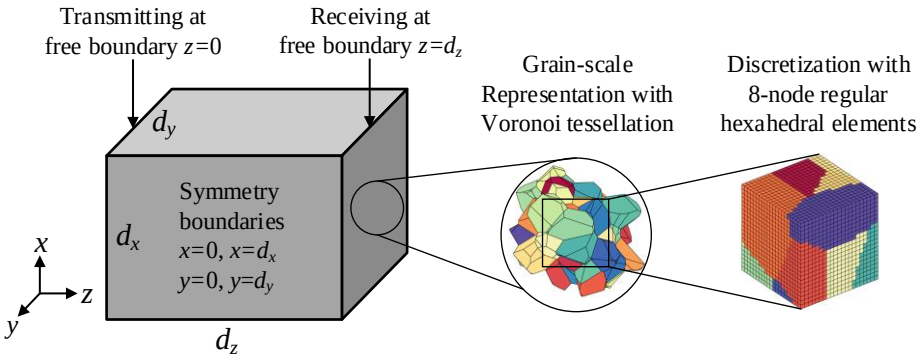


Fig. 1. (Color online) Illustration of the FE model for the propagation of plane longitudinal waves in polycrystals. The cuboid is the domain of modelling, having the dimensions of d_x, d_y and d_z in the x, y and z directions. The domain is partitioned into grains by using the Voronoi tessellation method. The grains are then divided into eight-node regular hexahedral elements, enabling the modelling of this complex problem by the FE method. Symmetry boundary conditions are imposed on the four external surfaces, $x = 0$, $x = d_x$, $y = 0$, and $y = d_y$, to emulate an infinitely wide model. A uniform dynamic force is applied to the transmitting surface of $z = 0$ to excite a plane longitudinal wave. In the through-transmission configuration, z-displacements are measured on the transmitting $z = 0$ and receiving $z = d_z$ surfaces to determine scattering parameters.

It is important to realize that every single model in Table I has a considerable sample volume and a large number of grains, but still, it is only an incomplete random realization (sample) of the parent polycrystal that one aims to simulate. Using a larger sample size and thus a larger number of grains can undoubtedly better represent the target polycrystal, but the massive sample size is

limited by computer memory, and often this is not as large as we would wish because of the intense demands on computer resources of the simulations. An alternative way of achieving a better representation is to use the combination of multiple realizations that are independently generated but follow the same statistics. This is comparable to multiple experimental measurements, performed at various locations of the same sample, that cover different volumes of grains. Multiple realizations can be generated by re-randomizing either grain seeds, crystallographic orientations, or both. It has been demonstrated[21] that these procedures are statistically equivalent, and this work uses the simplest one that reshuffles crystallographic orientations only.

Table I. Polycrystalline models. Dimensions $d_x \times d_y \times d_z$ (mm), number of grains N, average grain size a (mm), mesh size h (mm), degree of freedom d.o.f., center frequency of FE modelling f_c (MHz).

Model	$d_x \times d_y \times d_z$	N	a	h	d.o.f.	f_c	
						Aluminium	Inconel
N115200	12×12×100	115200	0.5	0.050	349×10^6	2, 5	2
N11520	12×12×10	11520	0.5	0.025	278×10^6	10	5
N16000	20×20×5	16000	0.5	0.020	755×10^6	20	10, 20

Table II. Polycrystalline materials. Elastic constants c_{ij} (GPa), density ρ (kg/m^3), anisotropy factor A, effective (Voigt) longitudinal and shear wave velocities $V_{\mathrm{L/T}}$ (m/s), and elastic scattering factors $Q_{\mathrm{L}\to\mathrm{L/T}}$ (10^{-3}).

Material	c_{11}	c_{12}	c_{44}	ρ	A	V_{L}	V_{T}	$Q_{\mathrm{L}\to\mathrm{L}}$	$Q_{\mathrm{L}\to\mathrm{T}}$
aluminum	103.40	57.10	28.60	2700	1.24	6317.52	3128.13	0.08	0.33
Inconel	234.60	145.40	126.20	8260	2.83	6025.37	3365.54	2.26	7.59

Thus, the present studies make use of a model volume that is inhomogeneous and anisotropic at grain scale, but homogeneous and isotropic in both stiffness and geometry at macro scale. However,

the principle established here may be extended to elongated grains and preferred crystallographic texture materials.

B. Approximation of wave equations by finite elements

The discretization of a volume of polycrystal material for the simulation of wave propagation has been discussed previously[21,31], and we follow closely the setup reported in Cook et al.[37]. The spatial representation process is illustrated in Fig. 1, with details in the caption.

While the spatial problem is represented by finite element discretization using first-order 8-node regular hexahedral elements, the time-stepping solution is based on the finite difference method, using the well-known equation:

$$\mathbf{M}\frac{\mathbf{U}^{n+1}-2\mathbf{U}^{n}+\mathbf{U}^{n-1}}{\Delta t^{2}}+\mathbf{K}\mathbf{U}^{n}=\mathbf{F} \tag{1}$$

in which Δt is the duration of discrete uniform time steps, the superscript n represents the current time step, $\mathbf{F}$ is the dynamic load vector describing externally applied forces at individual degrees of freedom, $\mathbf{M}$ and $\mathbf{K}$ are the mass and stiffness matrices, so $\mathbf{K}\mathbf{U}^{n}$ is the elastic force vector, with $\mathbf{U}^{n}$ representing the global displacement vector at time step n. $\mathbf{M}\ddot{\mathbf{U}}^{n}$ is the inertia force, and the acceleration vector $\ddot{\mathbf{U}}^{n}$ therein is represented by a standard central difference as $(\mathbf{U}^{n+1}-2\mathbf{U}^{n}+\mathbf{U}^{n-1})/\Delta t^{2}$. The equilibrium equation establishes the relation of displacements at three time steps $n-1$, n, and $n+1$. Re-arranging the equation allows the displacements at step $n+1$ to be determined explicitly from those already known at the two preceding steps. We neglect material damping in our studies.

The above FE formulation involves two major approximations that need to be carefully treated.

The first is the discretization of model space into elements, which we choose to be perfect identical cubes, all with an edge size of h, and this spatial discretization affects grain representation and numerical accuracy. The design of FE meshes to achieve a satisfactory convergence has been discussed widely in the literature, and it is important to note here that we limit our assessment to our specific present context of the solution of wave propagation in the time domain using the particular spatial and temporal schemes set out here. In other contexts the convergence can be quite different, for example Langer et al [38] show that several hundred elements per wavelength may be needed to achieve satisfactory convergence in the FE calculation of the eigenfrequencies of even a simple structure such as a plate in flexure. Structural vibration problems can incorporate quite complex spatial behavior that places additional demands beyond those of simple plane waves, and indeed this was demonstrated in the same paper by comparison of the plate flexural problem with a wave propagation problem that was much less demanding on spatial discretization. Furthermore, there are differences between the eigenvalue solution for frequency domain calculations and the time stepping for time domain problems.

In previous work using the same methodology as we discuss here, we found that a good representation of grains requires a minimum of 10 elements per average grain size a (specifically the cubic root of average grain volume) and a satisfactory numerical accuracy requires at least 10 elements per wavelength λ [21,31], the latter following on from previous work and prior reports by others. For now, we set out with this mesh refinement in mind, but we will evaluate in detail the accuracy both in wave velocity and wave amplitude in Sec. IV.A. We note that increasing either grain or wavelength sampling rate would help achieve better numerical accuracy and convergence but would also increase FE computation intensity, and 10 elements per grain dimension or wavelength is a moderate choice within our current computation capability. For the

231 former criterion, the required mesh size of a given polycrystal can be determined without
232 ambiguity from $a/h \geq 10$. For the latter, however, wavelength λ changes with frequency f
233 and phase velocity V. It is convenient to define a spatial sampling number as the ratio of
234 wavelength to mesh size, $S = \lambda/h = V/(fh)$. Thus, the latter discretization criterion can be re-
235 defined as $S \geq 10$, which should be met by the smallest wavelength that corresponds to the
236 highest simulation frequency and the slowest phase velocity.

237 The second approximation is the sampling of time into discrete steps with a spacing of Δt. This
238 temporal sampling and the spatial discretization collectively determine the stability of FE
239 calculations, which is prescribed by the Courant-Friedrichs-Levy condition. Due to the use of
240 explicit time-marching in Eq. (1), the condition of stability requires the Courant number being no
241 larger than unity, i.e. $C \leq 1$, which is to assure that the distance travelled by the wave in one time
242 step must not be greater than the distance between two mesh points. In the present work, the
243 Courant number is given by $C = V_{\max}\Delta t/h$, where $V_{\max}$ is the fastest phase velocity in the
244 simulated material, and for cubic materials considered in this work, it is given by[39] $V_{\max} =$
245 $\sqrt{(c_{11} + 2c_{12} + 4c_{44})/(3\rho)}$.

246 C. Excitation of plane longitudinal waves

247 Boundary and loading conditions are defined to excite the desired plane longitudinal waves, as
248 shown in Fig. 1, with details in the caption. The lateral boundary conditions that are prescribed so
249 that the finite domain represents an infinitely wide one can be achieved[21] by applying periodic
250 boundary conditions (PBCs) or symmetry boundary conditions (SBCs) to the four lateral
251 boundaries: $x = 0$, $x = d_x$, $y = 0$, and $y = d_y$. Both have been shown[21] to perform equally
252 well for polycrystals, and due to the ease of implementation in the FE method, the SBCs approach

is chosen in this work. The SBCs constrain the out-of-plane displacements of the lateral boundaries, i.e. $u_x(x = 0/d_x, y, z) = u_y(x, y = 0/d_y, z) = 0$.

Second, loading conditions are imposed to create longitudinal waves of plane wavefronts. This is implemented by applying a uniform dynamic force to the external surface of $z = 0$. A z-direction force, in the time domain being a three-cycle Hann-windowed toneburst of a center frequency of f_c, is exerted to all nodes on the surface $z = 0$. Due to the SBCs, this simulates a desired plane longitudinal wave travelling in the z-direction.

The time stepping solution to simulate the wave propagating through the polycrystal is hugely demanding on computers resources. For this reason, this work uses the GPU-based program Pogo[30], which can significantly accelerate the solving process in dealing with such large-scale problems[21].

III. EFFECTIVE MEDIA PARAMETERS FOR COHERENT WAVE: ATTENUATION AND PHASE VELOCITY

Although the initiation of the wave is coherent across the wavefront, the coherence is lost as the wave propagates through the polycrystal. The wavefront degenerates, scattering energy locally into incoherent diffuse components. Consequently, coherent waves are attenuated, and their phase velocities vary with frequency. These two scattering behaviors are parametrically described by attenuation coefficient $\alpha(f)$ and dispersive phase velocity $V(f)$, both as functions of frequency f.

A. Coherent waves

To calculate these two effective media parameters, displacements are numerically measured on planes normal to the propagation direction. In the case of plane longitudinal waves travelling in the z-direction as addressed in this work, z-displacements are acquired on cross-sections normal to the z-direction. Note that the displacement needs to be divided by 2 if the cross-section is the stress-free end at $z = d_z$, as the displacement is the sum of the incident and (equally) reflected waves. For an arbitrary cross-section $z = z_0$, the obtained displacement field is denoted as $u(x, y, z_0; t)$. The model length d_z for the z-direction will be used repeatedly hereafter, and for brevity, it will be simplified as d.

As a result of grain scattering, the phase of the wave $u(x, y, z_0; t)$ varies across points on the cross-section. The coherent part of this wave can be obtained by averaging this wave across the cross-section[40]; i.e. $U(z_0; t) = \langle u(x, y, z_0; t) \rangle_{x,y}$, where $\langle \cdot \rangle_{x,y}$ represents the spatial average over all points on the surface $z = z_0$. In the case of FE modelling, a significant number of nodes across the wavefront $z = z_0$ contribute to the average and thus a significant wave information is included in the coherent wave. Fourier transforming this coherent wave with respect to time t leads to its counterpart $U(z_0; f)$ in the frequency domain. Upon obtaining the coherent waves for two or more cross-sections, the two effective media parameters can be conveniently calculated which will be discussed in the following subsection.

In addition to the coherent part, there is the incoherent, fluctuation part in the total field $u(x, y, z_0; t)$ which scatters with a random phase across the wavefront and therefore its average over the cross-section is zero[40]. Although this fluctuation part is discarded in the calculation of effective media parameters, it is used below to demonstrate the level of scattering over a cross-section. For a clearer demonstration, the fluctuation part is normalized by the coherent part and

denoted as $u_{\mathrm{f}}(x, y, z_0; t) = [u(x, y, z_0; t) - U(z_0; t)]/U(z_0; t)$.

Here we use an example to illustrate coherent waves and fluctuations on wavefronts. The example simulates a plane longitudinal wave travelling in the model N11520 (Table I) using the material properties of Inconel (Table II). The wave is excited with a center frequency of 5 MHz. The z-displacement fields are recorded and denoted as $u(x, y, 0; t)$ and $u(x, y, d; t)$ for the transmitting $z = 0$ and receiving $z = d$ surfaces, respectively.

In the time domain, the spatial averages of the displacement fields, namely $U(0; t) = \langle u(x, y, 0; t)\rangle_{x,y}$ and $U(d; t) = \langle u(x, y, d; t)\rangle_{x,y}$, are calculated and plotted in Fig. 2(a). For these two coherent signals, Fig. 2(b) and (c) provide their corresponding fluctuations $u_{\mathrm{f}}(x, y, 0; t_1)$ and $u_{\mathrm{f}}(x, y, d; t_2)$ at the time instances of $t_1 = 0.30$ μs and $t_2 = 1.98$ μs, respectively. As shown in Fig. 2(a), the time instances t_1 and t_2 are chosen such that the coherent signals are at their maxima.

To obtain the spectral fields $u(x, y, 0; f)$ and $u(x, y, d; f)$, the time-domain fields are cropped by using the time windows that span from $t = 0$ to the vertical marks shown in Fig. 2(a) and then transformed to the frequency domain by utilizing the Fourier transform. Spatial averaging these spectral fields leads to the coherent parts $U(0; f) = \langle u(x, y, 0; f)\rangle_{x,y}$ and $U(d; f) = \langle u(x, y, d; f)\rangle_{x,y}$, whose amplitude spectra are plotted in Fig. 2(d). At the frequency of f_0 where the transmitting amplitude is at its maximum, the amplitude fluctuations $u_{\mathrm{f}}(x, y, 0; f_0)$ and $u_{\mathrm{f}}(x, y, d; f_0)$ are illustrated in Fig. 2(e) and (f).

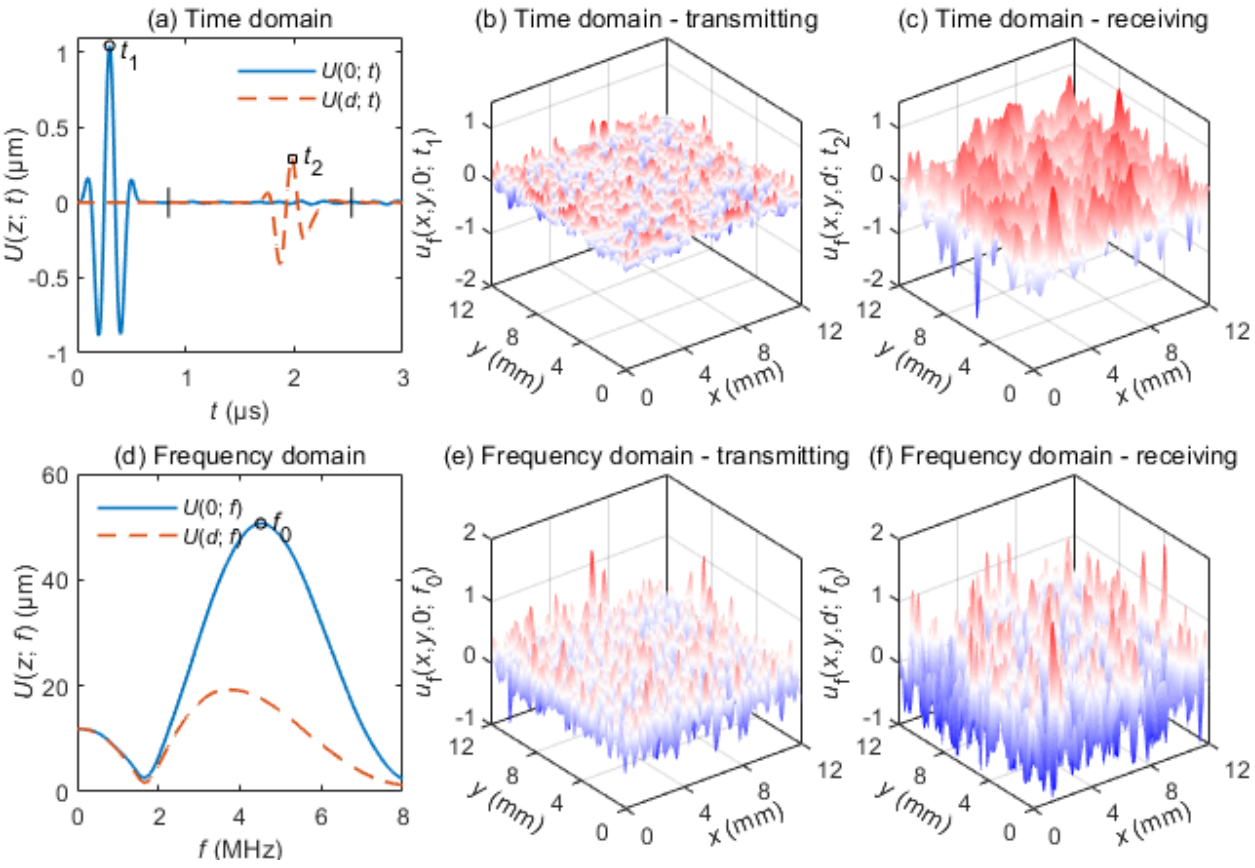


Fig. 2. (Color online) Illustration of coherent waves (a, d) and wavefront fluctuations (b, c, e, f) in the time (a-c) and frequency (d-f) domains, using the model N11520 with the material Inconel. The z-displacements are acquired on the transmitting $z = 0$ and receiving $z = d$ surfaces, leading to wave fields $u(x, y, 0; t)$ and $u(x, y, d; t)$. The solid and dashed lines in (a) are the spatial averages of these fields. (b) and (c) show normalized fluctuations $u_{\mathrm{f}}(x, y, 0; t_1)$ and $u_{\mathrm{f}}(x, y, d; t_2)$ for the transmitting and receiving surfaces, respectively; the time instances t_1 and t_2 are marked in (a). Similarly, (e) and (f) provide the normalized amplitude fluctuations at the frequency of f_0, which is marked in (d); these are obtained by performing Fourier transforms of the received signals at all points on the two cross-sections.

It is clear from Fig. 2(b) and (e) that the transmitting wavefront at $z = 0$ is not planar. This is because we apply forces on this plane and then measure displacements at the same location where

random elastic deformations occur immediately upon application of forces. As a result of multiple scattering, the field fluctuation on the receiving wavefront (Fig. 2(c) and (f)) is substantially larger than that of the source, leading to a smaller coherent wave (spatial average) on the receiving surface, as was seen in Fig. 2(a) and (d). As previously explained, the change of a coherent wave with propagation distance is represented by attenuation and dispersive phase velocity. The calculation of these parameters from the evolution of coherent waves will be addressed in the following subsection.

B. Determination of attenuation and phase velocity

Before determining the scattering parameters, we demonstrate how coherent waves change as they propagate through polycrystal media. In Fig. 3, example coherent waves in polycrystalline aluminum and Inconel are given as functions of propagation distances z. In the figure, a coherent wave $U(z;f)$ is normalized by its corresponding initiating wave $U(0;f)$, and the amplitude and phase parts of the normalized coherent wave, $U(z;f)/U(0;f)$, are denoted as $A(z;f)$ and $\varphi(z;f)$, respectively. These two parts are shown separately in the (a) and (b) panels of the figure.

Despite the large wavefront fluctuations (illustrated in Fig. 2), Fig. 3 shows that the amplitude and phase parts of the coherent wave change exponentially and linearly with propagation distance, respectively. It is important to emphasize that these exponential and linear relations are nearly perfectly described by their corresponding fitted straight lines (the goodness of fit is characterized by the annotated R^2 measure, and $R^2 = 1$ corresponds to a perfect fit). This is an essential evidence that the change of the coherent wave with distance can be very well represented by the effective media parameters, namely attenuation coefficient $\alpha(f)$ and phase velocity $V(f)$, by the following relations

$$A(z;f) = e^{-\alpha(f)z}, \quad \varphi(z;f) = \frac{2\pi f z}{V(f)} \tag{2}$$

It is clear from Eq. (2) that attenuation coefficient and phase velocity can be determined in two different ways; these will be described in the following subsections.

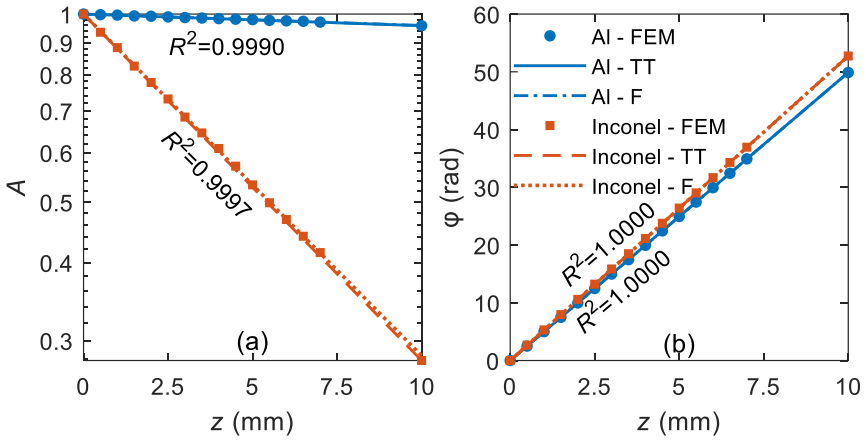


Fig. 3. (Color online) Amplitude and phase of typical coherent signals of polycrystalline aluminum and Inconel, normalized by the corresponding initiating waves $U(0;f)$. The signals are acquired from the model N11520 at the frequency of $f = 5$ MHz. (a) and (b) show the respective amplitude A and phase φ parts of the coherent waves. The solid (for aluminum) and dash (for Inconel) lines indicate the through-transmission (TT) method, and the dash-dotted (for aluminum) and dotted (for Inconel) represent the fitting (F) method in a least-squares sense. The through-transmission (TT) and fitting (F) lines are mostly overlapped. Part (a) of the figure uses the same legend as (b) and it uses a logarithmic y-axis scale. R^2 denotes the coefficient of determination that measures how successful a fitting (F) line is in explaining the variation of its corresponding FEM points ($R^2 = 1$ means a perfect fit).

1. Measurement by through transmission method

The first way to measure attenuation and phase velocity is to use only $U(0;f)$ and $U(d;f)$,

364 which are collected on the transmitting $z = 0$ and receiving $z = d$ surfaces, see Fig. 1. This
365 method is consistent with experiments where measurements can only be made on free boundaries.
366 This method is named the through-transmission method in this work and the two scattering
367 parameters can be given explicitly as

368 $$\alpha(f) = -\frac{\ln A(d;f)}{d}, \quad V(f) = \frac{2\pi f d}{\varphi(d;f)} \tag{3}$$

369 where $A(d;f)$ and $\varphi(d;f)$ are the amplitude and phase parts of $U(d;f)/U(0;f)$, respectively.
370 This method is graphically shown in Fig. 3 as the solid (for aluminum) and dash (for Inconel) lines
371 connecting the transmitting points at $z = 0$ to the receiving ones at $z = d = 10$ mm.

372 ## *2. Measurement by fitting method*

373 The second way is to use all the coherent waves, measured on free boundaries as well as inside
374 models. This can be fairly easily achieved by fitting the Eq. (3) to all the coherent waves, using
375 attenuation coefficient $\alpha(f)$ and phase velocity $V(f)$ as fitting parameters. Similarly, this
376 method is shown in Fig. 3 as the dash-dotted (for aluminum) and dotted (for Inconel) lines which
377 best fit all the data points in a least-squares sense.

378 ## *3. Comparison*

379 Previously, the authors[18,19,21,29,31] used the through transmission method, while Ryzy et
380 al.[32] employed the fitting method. In comparison, the results in Fig. 3 show a very small but
381 visible systematic difference for Inconel. The methods are further compared in Fig. 4 for aluminum
382 and Inconel over the frequency range of 3-6 MHz; details of the models are given in the caption.
383 Subtle differences can be observed between the two methods: for attenuation coefficient the
384 relative difference is smaller than 2% and for phase velocity it is smaller than 0.04%. Although

the differences are small, it seems that the through-transmission method gives systematically larger attenuation coefficients and smaller phase velocities than the fitting method. Thus, it is important to understand the reason for this seemingly systematic difference.

There are two key differences between these methods. 1) The through-transmission method uses waves collected on traction-free boundaries, while the majority of the waves of its counterpart are acquired inside models; this difference is illustrated in Fig. 5. Examples are provided in Fig. 6 to illustrate the difference between measurements made on boundaries and inside models. In the figure, circular data sets are acquired inside the model N11520 at the frequency of 5 MHz, with each point and error bar representing the mean and standard deviation of 15 realizations. Square data sets are collected on the same surfaces and under the same modelling conditions, but the collection surfaces are free boundaries which are formed by truncating the model N11520 at these measuring surfaces. Thus, the grains are identical for each of the two models under comparison at each propagation distance. The figure shows that the signal amplitudes on free boundaries are mostly smaller than those inside models, hence the resulting attenuation coefficient from through-transmission method is inevitably larger than that from the fitting.

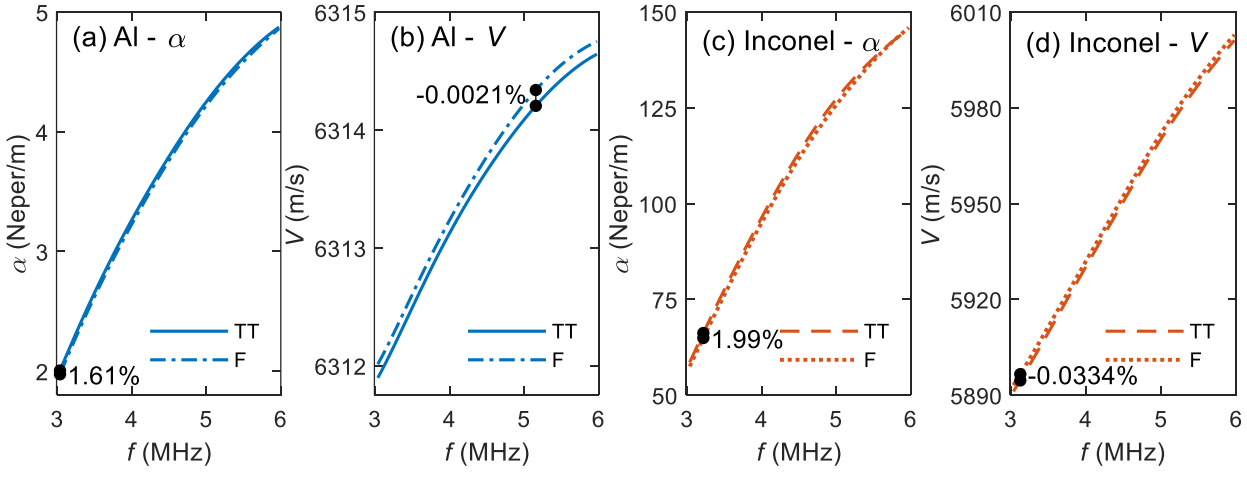


Fig. 4. (Color online) Longitudinal wave attenuations (a, c) and velocities (b, d) for polycrystalline

aluminum and Inconel determined by the through-transmission (TT) and fitting (F) methods. For each material we use 15 realizations of the model N11520 to get the averaged data as shown in the figure, and simulations are for a plane longitudinal wave with a center frequency of 5 MHz. The marks followed (or preceded) by percentages show the maximum discrepancies between the through-transmission (TT) and fitting (F) methods, with the fitting method as reference.

This difference is due to the fact that on boundaries and inside models, incoherent waves contribute to the coherent signals differently, see Fig. 5. It is not hard to imagine that on a measuring surface the incoherent waves induced by early arrivals enter the coherent part of the arrival signals. Inside models, coherent waves harvest incoherent ones in both forward- and backward-propagating directions, while on free boundaries incoherent backward-scattered waves are the main contributors. As a result, coherent waves collected inside models have slightly larger amplitudes than those acquired on the corresponding surfaces that are traction-free. Also, additional mode conversion of scattered waves on a free boundary may contribute to the difference. The incidence of random waves on complex free boundaries, with spatially-varied elastic properties, produces complicated reflections that involve mode conversions. Such mode conversions occur differently on a free boundary compared to the equivalent plane inside the material.

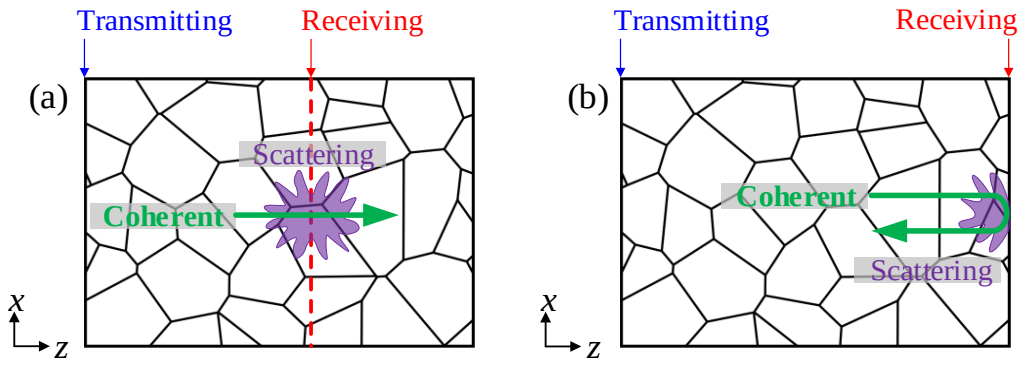


Fig. 5. (Color online) Illustration of collecting waves (a) on an internal cross-section and (b) on a

free boundary. The shown Voronoi diagram is the sectional view of a 3D polycrystal on the x-z plane. The transmitted coherent wave travels in the z-direction. In (a), the coherent wave received on the internal cross-sections acquires energy from the scattered waves that travel in both forward and backward directions. In (b), the coherent wave received on the free end is the sum of the incident and (equally) reflected waves, and this coherent part only incorporates the scattered waves that travel in the backward direction. Note that the number of grains in an actual simulation is far greater than that of the shown Voronoi diagram.

2) The second aspect is that the through-transmission method reflects the overall scattering behavior of the whole cuboid of a polycrystal medium, while its counterpart is largely influenced by the smaller subsets of the medium. It suggests that these two methods may have different statistical significances in representing the target polycrystal. This volume effect, however, is not the main cause of the difference between the two methods. The reason can be clearly seen from Fig. 6 which illustrates the use of identical volumes at each propagation distance still leads to statistically different results between the two methods.

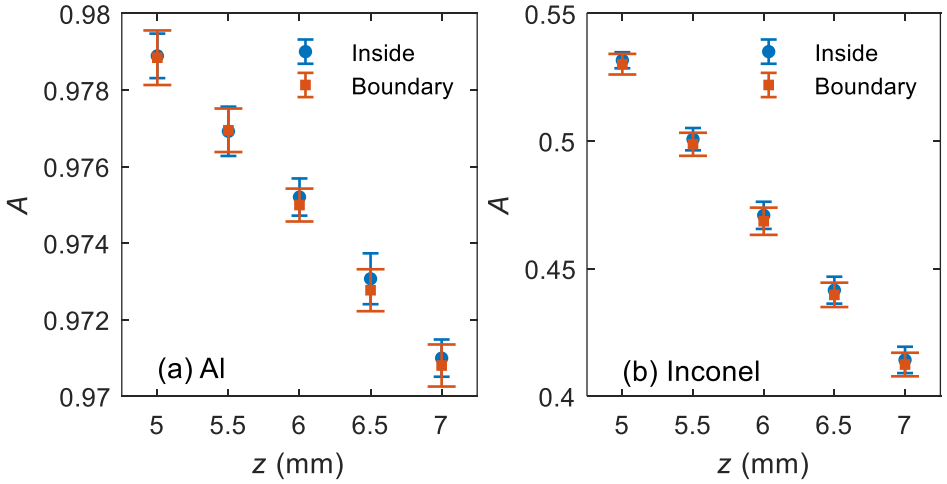


Fig. 6. (Color online) Coherent amplitudes of polycrystalline (a) aluminum and (b) Inconel measured inside FE models and on free boundaries. Amplitudes are plotted versus propagation

distance at the frequency of $f = 5$ MHz. Each material uses 15 realizations of the model N11520 to get the averaged data as shown in the figure. The circles represent signals collected inside the models, and the squares are collected on the same surfaces but the models are truncated at these surfaces to form traction-free boundaries.

However, it is important to realize that the difference between the two methods is generally within the range of error bars as shown in Fig. 6. This suggests that the through-transmission and fitting methods are practically equivalent and both can be used. In this work the through-transmission method is used in later discussions due to its convenience in the collection of waves and in the calculation of scattering parameters.

IV. NUMERICAL ERRORS AND STATISTICAL UNCERTAINTIES

It is certainly true that disagreement exists between results calculated by the FE method and the exact solutions. This disagreement should be estimated to establish the validity of the FE model and to aid improvement of its accuracy and precision.

In the case of modelling elastic wave propagation in polycrystals, the disagreement can be divided into two parts. One part is the systematic difference between an FE result and the exact solution, and another is the random variation around the FE result. These two parts are denoted as error and uncertainty, respectively. As mentioned in Sec. II.A, we obtain an FE result by averaging those of multiple FE realizations that are independently generated but follow the same microstructure statistic. Error in this case is the difference between the average result and the exact solution, while uncertainty is the standard deviation of the multiple results relative to the average. Error and

uncertainty arise in the FE model mainly as results of numerical approximations and statistical fluctuations.

Numerical approximations include two major facets: one is the approximation of an exact wave propagation problem by an FE model that is discretized in space and time, and another is the truncation or rounding of an exact number to a computer number that has a finite precision. These approximations cause numerical errors, and the estimation of these errors will be provided in Sec. IV.A.

Statistical fluctuations relate to the random nature of polycrystalline microstructure and the stochastic scattering it causes. A combination of multiple realizations is used in the FE model to average out the fluctuations and thus to obtain statistically meaningful FE results. Such statistical considerations are accompanied by statistical errors and uncertainties, which will be estimated in Sec. IV.B.

Following the estimations of errors and uncertainties in Sec. IV.A and Sec. IV.B, we examine in Sec. IV.C the propagation of errors and uncertainties through coherent waves to effective media parameters, namely attenuation coefficient and phase velocity. Finally, we provide examples in Sec. IV.D to illustrate some practical approaches to suppress errors and uncertainties. In this work, absolute and relative errors are denoted respectively as Δ and δ, while absolute and relative uncertainties are denoted as σ and ε.

A. Errors in numerical approximations

The spatial and temporal discretization approximations in the FE method introduce numerical errors, and here we look at both space and time. Our interest is to establish knowledge of the

underlying errors in amplitude and in wave velocity that come from the FE discretization of the propagation behavior; key to this is whether these errors are significant in comparison with, respectively, the changes of amplitudes due to scattering induced attenuation and the changes of phase velocity due to dispersion by the polycrystal. Such errors, if sufficiently understood, may also be used in practice in order to make corrections to simulated results. Therefore, we choose to assess the errors in a homogeneous isotropic domain, being the background on which the polycrystal behavior will be built, keeping with the same meshes and time stepping schemes of the latter. We recognize that this omits possible errors that might be specific to the discretization of the spatial changes in the polycrystal, but we suggest that the target of achieving good recommendations for choices of mesh and timestep is addressed most usefully by studying the non-specific homogeneous background case. Furthermore, we believe that a good discretization for the homogeneous background will automatically ensure good representation in the polycrystal case because it is already well established that the wave behavior is not sensitive to specific features at the space scale of the crystal boundaries, and indeed the analytical models do not include information about these boundaries at all[19].

The evaluation of the accuracy of FE models for wave propagation is a highly developed subject with a long history. Considerations of phase velocity dispersion in particular have motivated many different spatial and temporal schemes; dispersion is strongest for coarse meshes, so the challenge is to achieve best efficiency for a desired performance in modeling short wavelength waves. The monograph by Bathe[41] provides an excellent description and evaluation of the basic methodologies of the main schemes in use for time domain simulation. A variety of studies of performance of these and their variants, limiting to relevance to the method used in the present work, can be found in, e.g., [34,42–50].

We limit our reporting here to our specific choice of scheme and include results in brief for the benefit of modelers in the applications context of this article, leaving detailed evaluation of the mathematics and performance of the scheme to the cited literature. Our specific choice is the central difference explicit scheme, using lumped mass matrices, no material damping, and a structured mesh of identically-sized cube-shaped linear hexahedral elements. The basis of this choice has been optimized and explained in our previous work[21,31].

1. Analytical prediction of numerical errors

The exact solution to the propagation of elastic plane waves within an isotropic non-damping material is given by $\mathbf{u}(\mathbf{x},t)=\mathbf{p}_0\exp[i(\mathbf{k}_0\mathbf{x}-2\pi ft)]$, where $\mathbf{p}_0$ and $\mathbf{k}_0=k_0\mathbf{n}$ are the exact polarization and wave vectors, respectively. It is implied in the solution that the displacement amplitude is unity. There is no dissipation and the wave number $k_0=2\pi f/V_0$ is thus a real number, where V_0 is the exact phase velocity.

Due to numerical approximations, the FE solution to the same problem is approximate. At a given node $\mathbf{x}$ and time instance $t=n\Delta t$, the approximate solution $\mathbf{u}_\mathbf{x}^n$ takes a similar form to the exact one

$$\mathbf{u}_\mathbf{x}^n=\mathbf{p}e^{i(\mathbf{k}\cdot\mathbf{x}-2\pi fn\Delta t)} \tag{4}$$

where $\mathbf{p}$ and $\mathbf{k}=k\mathbf{n}$ are the approximate polarization and wave vectors. Numerical attenuation α, if any, and phase velocity V are included in the complex wave number k, i.e. $k=2\pi f/V+i\alpha$. By using Eq. (3), the wave number can be further related to amplitude and phase changes via $k=\varphi/d-i\ln A/d$, where d is the wave propagation distance. Thus, the estimation of amplitude and phase errors depends on the solution of wave number k.

The central difference explicit scheme is known to be non-dissipative, correctly conserving the energy of the propagating waves [49,50], although the literature devotes little attention to the details of this, concentrating in preference to the real concern, which is the velocity dispersion. Here we suggest it is useful to think a bit more about the non-dissipative property before we look at the dispersion.

The non-dissipative property can be examined by looking at the numerical wave propagation solution for a monochromatic plane wave in an infinite domain (see also, e.g., [43,50]). The elements are all identical, so we arbitrarily consider a single node, with waves propagating in the z direction and no external forces. The scheme requires only local information at each time step, so we need only consider information from the eight elements that adjoin this node. This local assembly has mass $\mathbf{M}$ and stiffness $\mathbf{K}$ matrices with 81×81 coefficients, as defined in Sec. II.B.

Substituting Eq. (4) into Eq. (1) gives a system of 81 equations. However, the eight-element assembly only carries complete information of nodal connectivity for the target node. As a result, only the three equations which correspond to the degrees of freedom of this target node are meaningful in terms of describing wave motion, and, considering compression waves, only the displacement in the chosen coordinate z relates to the example wave propagating along z. Simplifying this equation results in

$$(e^{-i2\pi f\Delta t} + e^{i2\pi f\Delta t} - 2)h^2 - (e^{-ikh} + e^{ikh} - 2)V_0^2\Delta t^2 = 0 \tag{5}$$

and solving this equation leads to

$$k = \frac{1}{h}\arccos\left[\frac{\cos(2\pi f\Delta t)-1}{V_0^2\Delta t^2}h^2 + 1\right] \tag{6}$$

It is clear from Eq. (6) that k is a real number. This confirms the non-dissipative nature of the

solution, which holds for plane waves that are continuous in space and time. A similar analysis would show the same for shear waves.

Eq. (6) also shows the relative phase error, which is given by $\delta_\varphi = (k - k_0)/k_0$. We define the spatial sampling and Courant numbers with respect to the longitudinal phase velocity $V_0 = V_\mathrm{L}$, i.e. $S = V_\mathrm{L}/(fh)$ and $C = \Delta t V_\mathrm{L}/h$. Considering these relations, relative phase error can be expressed as

$$\delta_\varphi = \frac{S}{2\pi}\arccos\left[\frac{\cos(2\pi C/S)-1}{C^2} + 1\right] - 1 \tag{7}$$

The equation shows that phase error is directly related to spatial sampling number S and Courant number C, which correspond to spatial discretization and time stepping respectively. It follows now that we also have anisotropic behavior because, however well the element behaves for waves at different angles, the spatial sampling is certainly different in different directions; this is a well-known property of these solutions[34,43,47]. Thus we see that we should expect perfect preservation of the amplitude of monochromatic plane waves, but a frequency-dependent error of phase velocity. The latter will imply that the amplitude of the envelope of a wave packet in the time domain will in general exhibit distortion as it travels. We will evaluate this performance in simulation studies in the following two sub-sections.

2. Evaluation of numerical phase errors

A simple cuboid model, with the dimensions of $d_x \times d_y \times d = 12 \times 12 \times 10$ mm, is established using isotropic steel, with Young's modulus $E = 210$ GPa, Poisson's ratio $\nu = 0.3$ and density $\rho = 8000$ kg/m^3. The longitudinal wave velocity of this material is $V_\mathrm{L} = 5944.45$ m/s. Similar to the FE model given in Sec. II, the model is discretized with uniform eight-node cube elements

and configured to accommodate a plane longitudinal wave that has the center frequency of 5 MHz. The transmitting and receiving waves, $U(0,f)$ and $U(d,f)$, are collected and the relative phase error is thus obtained as $\delta_\varphi = \varphi/(2\pi f d/V_\mathrm{L}) - 1$, where φ is the phase part of $U(d,f)/U(0,f)$.

Fig. 7 compares the actual simulations with analytically predicted results from Eq. (7). The left panel (a) assesses the influence of spatial discretization, as characterized by sampling number S, while the right panel (b) evaluates the impact of time stepping, as characterized by the Courant number C. Model details are given in the figure caption. The figure shows that actual phase errors can be well represented by Eq. (7).

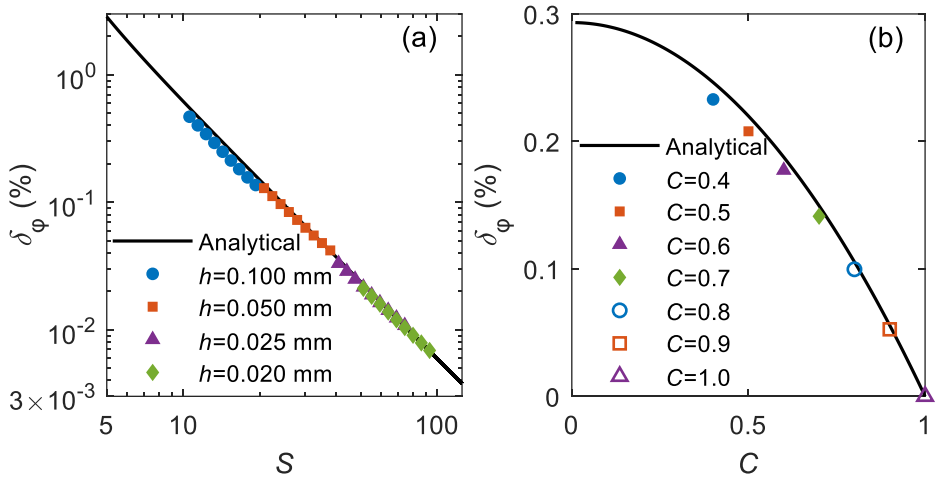


Fig. 7. (Color online) Evaluation of numerical phase errors. (a) and (b) assess the influences of spatial sampling number S and Courant number C, respectively. (a) uses four models with different mesh sizes, $h = 0.100, 0.050, 0.025, 0.020$ mm, and fixed Courant number, $C = 0.8$. The resulting relative phase errors (points) are plotted against their sampling numbers S in the frequency range of $f = 3 - 6$ MHz. (b) uses seven models with fixed mesh size, $h = 0.025$ mm, and different Courant numbers, $C = 0.4, 0.5, \ldots, 1.0$. Their relative phase errors (points) are plotted versus their Courant numbers at the frequency of $f = 5$ MHz. The solid lines in (a) and

581 (b) are analytically predicted errors from Eq. (7). Note that the vertical y axes in the figure panels
582 show the percentage error over the propagation distance of 10 mm.

583 A key observation from the figure is the high degree of accuracy of the calculated phase. The
584 lowest sampling number, S, in the results in part (a) of the figure is 10 elements per wavelength,
585 for which the phase error (and thus velocity error) is about 0.5%, and this error is reduced to 0.1%
586 by increasing S to 20 elements per wavelength. Thus, the policy of using at least 10 elements per
587 wavelength is justified for all routine analysis by this method unless particularly high precision is
588 to be pursued.

589 The figure also defines the two approaches to reduce phase errors, pertaining to spatial
590 discretization and time sampling, respectively. The first is to use finer meshes, which can be
591 discovered from the left panel (a) that phase error decreases exponentially ($\delta_\varphi \propto \exp(-2S)$) as
592 spatial sampling number increases. The second approach is to use larger Courant numbers, which
593 can be found from the right panel (b). When this number is at its limit of unity, phase error can
594 nearly be removed. However, for stability reasons it is not recommended to use $C = 1$ because
595 the actual C in a simulation could be greater than 1 (thus violate the stability condition) as a result
596 of accelerated wave velocity caused by numerical dispersion, and also this condition cannot be
597 achieved for all waves when there are spatial variations of material properties or multiple wave
598 modes. An important implication of the second approach is that a structured mesh is likely to
599 perform better than a free mesh in this analysis. This is because the free mesh has a range of
600 element sizes and the range can be very wide for sharp spatial features, and therefore it is
601 impossible to achieve the same Courant number everywhere, even if there is only one wave mode
602 and material present. In Sec. IV.D.1, examples will be given to show actual errors in phase velocity
603 calculations and to illustrate the corrections of these errors by using the two approaches discussed

here.

3. Evaluation of numerical amplitude errors

We use the same models as for Fig. 7(a) and calculate their relative amplitude errors by $\delta_A = A - 1$, where A is the amplitude of $U(d,f)/U(0,f)$ and its exact solution is unity in the absence of amplitude error. In the frequency range of $f = 3 - 6$ MHz, the errors are plotted against frequency in Fig. 8.

Fig. 8 shows that the amplitude errors of the FE simulations are small, and that they reduce as the mesh is refined, but they are not zero. We recall here that we expect zero loss for monochromatic plane waves, but that analysis did not include the FE calculations for the transient behavior of a wave packet. Critically, we need to distinguish here between energy loss, which would violate the non-dissipative nature, and signal distortion without loss of energy. Therefore, we have calculated the integral of the energy content for the whole wave packet in each case and this revealed that the energy loss is negligible, at around 10^{-4} % for the coarsest mesh. Thus, what we see here is that the energy is correctly retained, so the solution is convincingly non-dissipative, but that there is some small distortion of the amplitude spectrum, resulting in time-shifting of some spectral amplitudes in the wave packet.

For interest, Fig. 8 also shows the normalized amplitude spectrum of the transmitting wave for the model with the mesh size of $h = 0.100$ mm, which can be seen, when scaled appropriately (right *y*-axis), to match the same shape as the spectrum of the distortion. Further work on this observation could be academically interesting, but this would be beyond the present scope. For now, we note that the wave packet does not dissipate energy, but that there is a small distortion across the amplitude spectrum; furthermore, the latter is very small (0.2%), even for the coarsest mesh ($S =$

12 elements per wavelength at center frequency), while for the preferred finer meshes it is below 0.003% across the bandwidth ($S = 60$ elements per wavelength at center frequency). These are very small numbers compared to the scattering induced attenuation in the polycrystal.

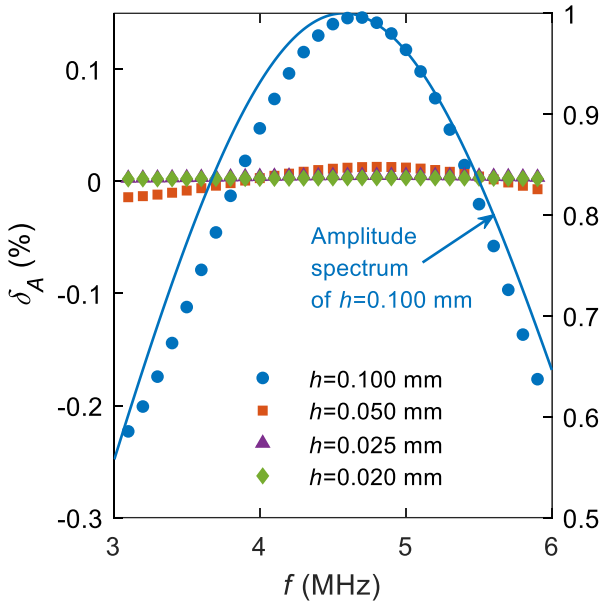


Fig. 8. (Color online) Evaluation of numerical amplitude errors. The evaluation utilizes the four FE models that are used in Fig. 7(a). The points represent the relative amplitude errors and they use the left y-axis. The solid line is the normalized amplitude spectrum of the transmitting wave for the model with the mesh size of $h = 0.100$ mm and it uses the right y-axis. Note that the vertical y axes in the figure panels show the percentage error over the propagation distance of 10 mm.

Thus the analysis and practice both show that amplitude errors are insignificant in comparison to phase ones. Therefore we can expect that limitations of the FE modelling will impact the predicted phase velocity but have negligible influence on the wave amplitude when reported in the frequency domain. The key result to achieve accurate simulation is the phase error in Fig. 7(a), showing dramatic improvement as the number of elements per wavelength, S, is increased. However, this

is in direct conflict to the desire to minimize S for large models and high frequency simulations.

B. Errors and uncertainties in statistical considerations

Generally, we aim to simulate polycrystals of prescribed statistical properties. A single FE model is not capable of fully describing one of such polycrystals, due to its relatively small sample volume and finite number of grains. Instead, the statistical combination of the results of multiple realizations that are randomly generated following the same statistical property are desirable to draw meaningful conclusions about the given polycrystal.

The effectiveness of using multiple realizations to achieve statistical convergence is exemplified here. The model N11520 is used to simulate polycrystalline aluminum and Inconel that have statistically isotropic and macroscopically homogeneous properties. Due to random scattering, the wave field $u(x, y, d; t)$ on the receiving plane $z = d$ should be randomly distributed. This means that at a given time instance of $t = t_0$ the fluctuation $u_{\mathrm{f}}(x, y, d; t_0)$, which is defined in Sec. III.A, should follow the Gaussian distribution. However, the actual distribution of a single realization differs from the Gaussian for both aluminum and Inconel, which are respectively shown in Fig. 9(a) and (b) as probability density histograms. Instead, the combination of multiple realizations (15 in this example) delivers satisfactory distributions that agree very well with the Gaussian. Thus, a combination of multiple realizations can be regarded a confident description of the target polycrystal.

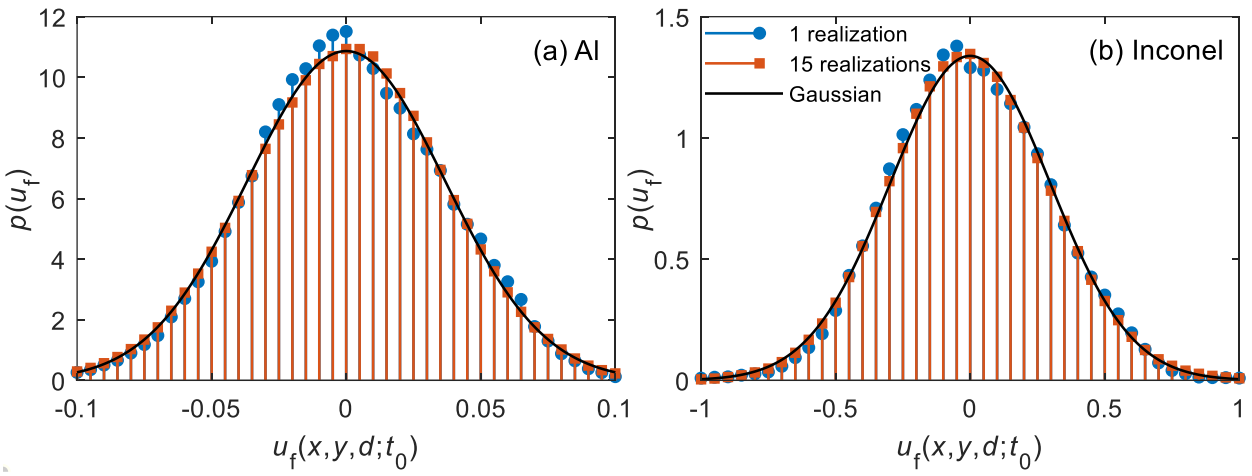


Fig. 9. (Color online) Probability density of the normalized receiving fluctuation fields of (a) aluminum and (b) Inconel. The materials are simulated using the model N11520 with the center frequency of 5 MHz. Each realization is independently generated by randomizing its crystallographic orientations. The fluctuation $u_f(x, y, d; t_0)$ of each realization is collected at all nodal points on the receiving plane $z = d$. The time instances t_0 for aluminium and Inconel are 1.88 and 1.98 μs respectively, which correspond to the maxima of their coherent waves $U(d; t)$. Note the order of magnitude difference in the horizontal scale indicating significantly stronger scattering for Inconel. Part (a) uses the same legend as (b).

As mentioned in Sec. III.A, we use the coherent wave of a model to calculate effective media parameters. In the case of multiple realizations, the calculation needs to use the average of the multiple coherent waves that can be denoted as $\mu(z; f) = \langle U_i(z; f)\rangle_i$, where $U_i(z; f)$ is the coherent wave of the i-th realization. As prescribed by the central limit theorem, the multiple coherent waves follow the Gaussian distribution because the multiple realizations are independently randomly generated. And, the average $\mu(z; f)$ is an appropriate estimate of the true coherent wave, and this estimation includes statistical uncertainty and error as discussed below.

Uncertainty is characterized by the standard deviation $\sigma(z; f)$ of the coherent waves. Here we

use the 15-realization example of Fig. 9 to investigate the uncertainties associated with our simulations. For the received coherent waves $U_i(d;f)$ $(i = 1,2,\ldots,15)$, their uncertainties are calculated and split into amplitude σ_A and phase σ_φ parts, respectively; normalization by their respective mean values results in relative uncertainties $\varepsilon_A = \sigma_A/\mu_A$ and $\varepsilon_\varphi = \sigma_\varphi/\mu_\varphi$. The results show that Inconel has a larger uncertainty than aluminum, which is consistent with Fig. 9. This means that uncertainty is positively correlated with material anisotropy. In addition, the amplitude uncertainty is around 10 times larger than that of phase. This is opposite to what we found for numerical errors which was that amplitude error is in general smaller than phase error; this was shown in Fig. 8(b).

Error in this case is termed the standard error of the mean. It is a statistical error between the mean and the true value, and it can be probabilistically estimated by $\sigma_\mu = \sigma/\sqrt{N}$, where N is the number of realizations.

It is important to realize that uncertainty cannot be suppressed, but rather it can be better determined by using more realizations for example. For standard error, however, its expression indicates that it can be reduced by increasing the number of realizations N. Practically, a simple trial-and-error process can be employed to suppress standard error to a satisfactory extent. This process increases the number N until the relative standard error of either amplitude or phase ($\delta_\mu = \varepsilon_{A,\varphi}/\sqrt{N}$) is below a set threshold (e.g. 0.1%).

C. Propagation of errors and uncertainties

It is known that errors and uncertainties propagate through independent variables to dependent ones. Thus, those of coherent waves discussed in Sec. IV.A and Sec. IV.B will be brought into

scattering parameters, namely attenuation coefficient and phase velocity, via Eq. (3).

Given that propagation distance and frequency are accurate, the attenuation coefficient in Eq. (3) is a univariate function of amplitude. We denote amplitude error as $\Delta_A = A - A^{\mathrm{T}}$, where A^{T} is the true amplitude and A is its estimation given by the mean of multiple realizations. Replacing A by A^{T} in Eq. (3) and expanding this equation about the point A in a Taylor series, we can then obtain the relative error of attenuation coefficient

$$\delta_\alpha = -\frac{e^{\alpha d}}{\alpha d}\Delta_A + O[\Delta_A^2] \tag{8}$$

where α is the true value of attenuation coefficient; frequency f is implicit. In general, the true attenuation coefficient α is unknown, so instead it is approximately replaced by the mean value of multiple realizations. Note that only the first-order term of the Taylor expansion is used in the equation, by assuming that amplitude error is small. Higher-order terms should be included if this assumption does not hold. For uncertainty, we need to express the attenuation coefficient of each realization as a Taylor series. Substituting the expansion into the formula of standard deviation, we can then obtain the relative uncertainty

$$\varepsilon_\alpha = \frac{e^{\alpha d}}{\alpha d}\sigma_A + O[\sigma_A^2] \tag{9}$$

where σ_A is amplitude uncertainty. Similarly, assuming that phase error and uncertainty are small, then their propagation from phase to velocity can be easily obtained from Eq. (3)

$$\delta_V = \frac{V}{2\pi f d}\Delta_\varphi + O[\Delta_\varphi^2], \quad \varepsilon_V = \frac{V}{2\pi f d}\sigma_\varphi + O[\sigma_\varphi^2] \tag{10}$$

where V is the true phase velocity that is approximated to the mean value of multiple realizations.

As shown in Eqs. (8) and (9), the error and uncertainty of attenuation coefficient are related to those of amplitude by the same factor, $F_\alpha = \exp(\alpha d)/(\alpha d)$. Due to the lack of true values, such propagation of error cannot be evaluated. However, it is easy to do so for uncertainty. For this purpose, σ_A and ε_α are calculated from 15 realizations and the actual propagation factor is calculated from their division. The resulting factor is plotted against αd in Fig. 10(a) for aluminum and Inconel, and each material covers a wide frequency range by using three models: N115200, N11520 and N16000. The actual uncertainty propagation can be seen to be very well represented by the analytical factor F_α, and this should always be valid as long as amplitude uncertainty is small. Likewise, this factor is also applicable to error propagation on the same condition that amplitude error is small. The figure conveys an important information that the propagation factor is at its minimum of $e = 2.72$ when $\alpha d = 1$ Neper. Thus, in order to suppress the magnification of error and uncertainty, the total attenuation αd should be kept around 1 Neper[51]. Practically, we have observed that moderate magnifications can be achieved by maintaining αd between 0.01 and 6 Neper.

For phase velocity, Eq. (10) show that the same factor $F_V = V/2\pi f d = 1/\varphi$ governs both error and uncertainty propagation. Similarly, uncertainty propagation is evaluated in Fig. 10(b) by using the same models as its left panel. The figure shows that the factor F_V agrees very well with actual simulations, and it is no doubt that it is also valid to error propagation. An elaborate analysis would suggest that error and uncertainty are naturally suppressed during their propagation. This is based on the fact that achieving a good statistical significance requires waves to propagate at least a quarter of wavelength, which means $\varphi \geq 2\pi/4 = \pi/2$ and further leads to $F_V = 1/\varphi \leq 2/\pi < 1$. We note that in Fig. 10(b) the phase φ on the horizontal axis is in the range from 10 to 1000 and the propagation factor F_V on the vertical axis is not greater than 0.1. It is also important to

emphasize that better suppression can be achieved by using a longer model length d. However, increasing d can make it difficult to meet the condition of αd being close to 1 Neper, which is necessary to suppress the error and uncertainty of attenuation. It is thus advised to only consider the suppression condition exerted to attenuation and that of phase velocity should be fulfilled accordingly.

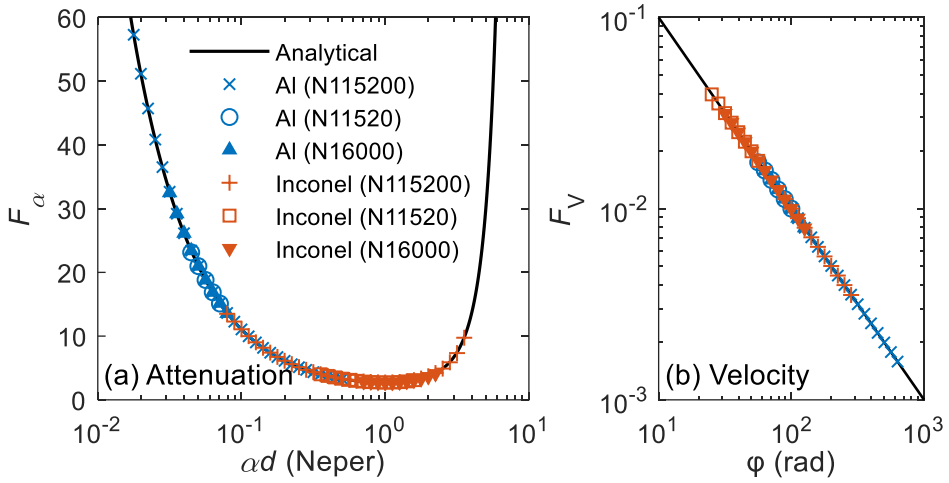


Fig. 10. (Color online) Propagation factors for the uncertainties of (a) attenuation and (b) phase velocity. Lines represent analytically derived factors, while the points are obtained from 15 FE realizations. For aluminum, the models N115200, N11520 and N16000 cover the frequency ranges of 1-6.5, 6.5-13.5 and 13.5-25 MHz, respectively. For Inconel, the ranges are 1-2.5, 2.5-6.5 and 6.5-23 MHz. Part (b) of the figure uses the same legend as (a).

D. Example suppression of errors and uncertainties

The preceding studies have provided a variety of ways to understand and then suppress errors and uncertainties. Following these studies, this subsection presents some typical examples to demonstrate the practical use of the suppression methods in actual simulations.

Suppressing statistical error and uncertainty is relatively simple, and it is thus not exemplified in

this subsection. As illustrated in Sec. IV.B, statistical error can be reduced to a satisfactory extent by increasing the number of realizations N, while uncertainty cannot be suppressed and can only be better determined through the use of large N. For all simulations considered in this work, we use $N = 15$ to achieve a satisfactory statistical error of at most 0.1% and a sufficiently good determination of uncertainty. Sec. IV.C further suggests that the propagations of statistical error and uncertainty can be effectively suppressed by minimizing the factors F_α and F_V, respectively. But because such minimization equally suppresses numerical errors, we leave its discussion to the following example suppressions of numerical errors.

Suppressing numerical errors requires a good combination of modelling parameters, and the suppression approach differs from phase velocity to attenuation. Thus, the following gives suppression examples separately for velocity and attenuation.

1. Suppression of numerical velocity errors

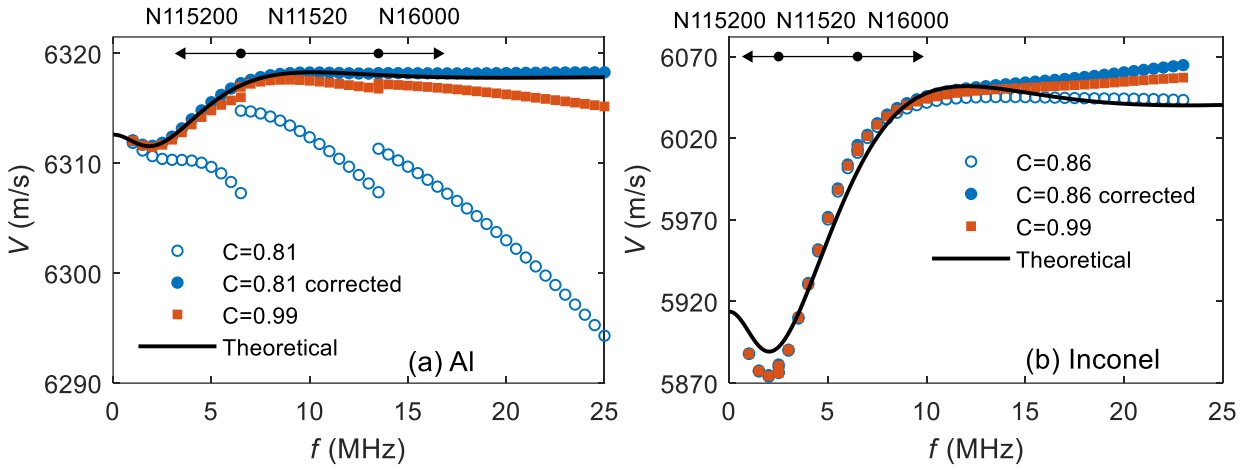
As shown in Eq. (10), the relative error of phase velocity δ_V is the product of phase error Δ_φ and propagation factor F_V. Thus, reducing either of these two parts leads to the suppression of velocity error. For F_V, Sec. IV.C infers that it naturally reduces errors as it is smaller than unity. This factor can be further reduced by using a longer model length d. However, we do not aim to do so, because d is a critical parameter for suppressing attenuation error.

For Δ_φ, we have obtained its analytical expression for homogeneous materials as given in Eq. (7). Although we have not seen a means yet to extend it analytically to polycrystals, we shall see that the conclusions drawn from it can be quantitatively applied to polycrystals for error suppression. To use this equation for polycrystals, we define its spatial sampling number S with respect to the Voigt velocity V_L, i.e. $S = V_\mathrm{L}/(fh)$, and its Courant number C with respect to the peak velocity

$V_{\max}$, namely $C = \Delta t V_{\max}/h$. For cubic materials considered in this work, the Voigt and peak velocities are given respectively as $V_{\mathrm{L}} = \sqrt{(3c_{11} + 2c_{12} + 4c_{44})/(5\rho)}$ [19] and $V_{\max} = \sqrt{(c_{11} + 2c_{12} + 4c_{44})/(3\rho)}$ [39].

Reducing phase error Δ_φ can be achieved by using the two approaches summarized in Sec. IV.A.2. The first approach is to use a larger spatial sampling number S. However, this approach is practically difficult for the present example. This is because the three material models (Table I) used in this work are already very big in terms of their required computational resources, and further increasing their S requires the use of even finer meshes that would easily exceed our current computer capability. Instead, this first approach is substituted by a correction approach that uses the numerical phase error predicted from Eq. (7) to correct the error included in simulation result. The second approach is to control phase error Δ_φ by using a Courant number which is as close to unity as possible.

Examples are provided in Fig. 11 to illustrate these two approaches. The examples use the same FE models and configurations as Fig. 10. In the figure, the phase velocities obtained from FE simulations are provided as discrete points, and theoretically predicted results are given as lines. The accurate statistical information of the FE material models is incorporated into the theoretical curves (see Sec. V for details), and these curves are of good accuracy for the studied materials and frequency ranges. In particular, the curve of aluminum in panel (a) is very accurate because the underlying theory can take almost all its weak scattering into consideration. This curve can thus be used as a reference to evaluate the error suppression approaches.



797

798 Fig. 11. (Color online) Example suppression of numerical velocity error for polycrystalline (a)
799 aluminum and (b) Inconel. Lines represent theoretically predicted[18] phase velocities, while
800 points are obtained from 15 FE realizations. Hollow circles represent un-corrected results and their
801 corrected ones are shown as solid circles. Solid squares represent results obtained by using larger
802 Courant numbers. For aluminum, the models N115200, N11520 and N16000 cover the frequency
803 ranges of 1-6.5, 6.5-13.5 and 13.5-25 MHz, respectively. For Inconel, the ranges are 1-2.5, 2.5-6.5
804 and 6.5-23 MHz.

805 For the first approach of error correction, phase velocities before correction are provided as hollow
806 circles and corrected ones as solid circles. In this case, small Courant numbers (0.81 for aluminum
807 and 0.86 for Inconel) are used in order to get large phase errors and thus to show clear effects of
808 correction. The correction is achieved by subtracting the numerical phase error $\varphi\delta_\varphi$ (δ_φ is the
809 relative phase error calculated by Eq. (7)) from the simulation result φ and then calculating the
810 corrected phase velocity by $V = 2\pi fd/(\varphi - \varphi\delta_\varphi)$. It is obvious that before correction, the three
811 models (N115200, N11520, N16000) do not give consistent velocities as expected at the transitions
812 between individual models. Note that the transitional inconsistency is less clear for Inconel (panel
813 (b) of the figure) because its y-axis scale is too large to show this. This inconsistency is nicely

averted in the corrected results, implying the effectiveness of the correction approach. Also, by comparing the hollow and solid circles with the theoretical curve of aluminum (panel (a)), we can observe that the use of the correction approach significantly suppresses numerical phase velocity errors.

For the second approach of error control, both aluminum and Inconel use a large Courant number of $C = 0.99$. This is the largest C number attempted in this study that does not encounter stability issues; the Courant numbers above $C = 0.99$ were tested but led to unstable FE computations for both aluminum and Inconel. The velocity results are provided in the figure as solid squares. The results show good consistencies at model transitions, but not as good as the corrected results of the first approach. The theoretical curve of aluminum in panel (a) is also closer to the corrected points, suggesting that the correction approach performs better than the control approach. This error control approach, however, may be more advantageous for practical simulations as it requires less post-simulation calculations compared to the correction approach.

2. Suppression of numerical attenuation errors

Eq. (8) indicates that the relative error of attenuation δ_α is the multiplication of amplitude error Δ_A and propagation factor F_α, and thus reducing either of these two parts leads to the suppression of attenuation error. It is suggested in Sec. IV.A.3 that amplitude error Δ_A can be reduced by using either a larger spatial sampling rate S (thus a finer mesh size h) or an appropriate spectrum range that is in close proximity to its maximum. And Sec. IV.C indicates that propagation factor F_α can be suppressed by limiting αd to a certain range in the vicinity of 1 Neper.

Thus, three opportunities are available to suppress numerical attenuation errors. For the first opportunity of using a larger spatial sampling rate S, we have mentioned above in Sec. IV.D.1

that the three models utilized in this work are already very computationally intensive, and therefore we do not aim to further increase their sampling rates. For the third opportunity of using a αd being close to 1 Neper, the creation of the currently used FE models has ensured that this condition can be relatively easily satisfied. It is certainly true that we can create more models to accommodate different modelling frequencies and polycrystalline media, such that we always have an optimal suppression condition of $\alpha d \approx 1$ Neper. But such treatment would introduce huge computation and time costs, and therefore it is not pursued in this example. Instead, this example uses a combination of all three opportunities, rather than any single one, to reduce attenuation errors.

The principle of combining the suppression opportunities is relatively simple. For a given material, trial simulations (or theoretical predictions) are first conducted to determine the frequency range of each FE model in which αd is within a bound of 1 Neper, e.g. $0.01 \leq \alpha d \leq 6$ Neper. If there is an overlapped frequency range between two models, the overlapped range is designated to the model with either a larger sampling rate S, a closer attenuation αd to 1 Neper, or both. Finally, within the chosen frequency range of each model, transmitting center-frequencies are tailored to ensure that the whole range use appropriate spectra of the waves.

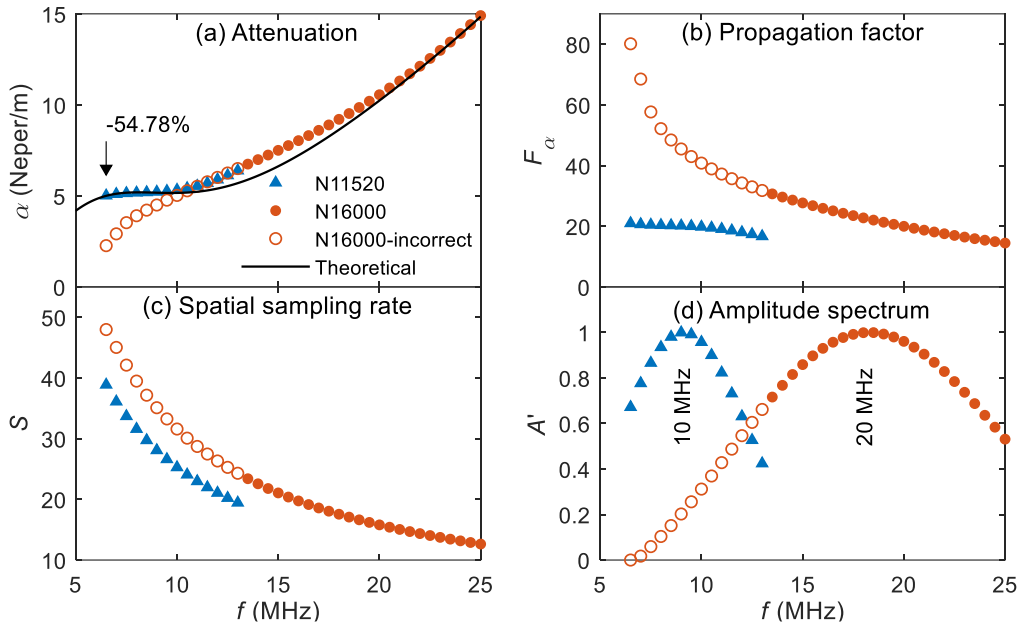


Fig. 12. (Color online) Example suppression of numerical attenuation error for aluminum. (a) shows attenuation coefficients obtained from FE models (points) and a theoretical model[18] (solid line). Solid points represent satisfactory results with attenuation errors being appropriately suppressed, while incorrect results are plotted as hollow circles. (b) gives the error propagation factors for the FE models, $F_\alpha = \exp(\alpha d)/(\alpha d)$. (c) plots the spatial sampling rates $S = V_{\mathrm{L}}/(fh)$ and (d) the normalized transmitting amplitude spectra $A' = A(0;f)/\max(A(0;f))$. All panels (b)-(d) use the same legend as given in (a). Each FE model uses 15 realizations to get the averaged result as shown in the figure.

Here we provide an example in Fig. 12 to demonstrate an incorrect combination of suppression opportunities and the corrected combination that appropriately reduces numerical attenuation errors. The example is given for the material of aluminum. In the frequency range of 6.5-13.5 MHz, panel (b) shows that the models N11520 (solid triangles) and N16000 (hollow circles) both satisfy the condition of $0.01 \le \alpha d \le 6$ Neper ($2.72 \le F_\alpha \le 101.00$). The incorrect combination chooses the model N16000 to cover this frequency range because it has a larger sampling rate S

than N11520, which is shown in panel (c). To save modelling costs, the incorrect combination excites a transmitting wave, in the form of a three-cycle Hann-windowed toneburst, with a center frequency of 20 MHz to provide a wide frequency coverage. In this case, the range of 6.5-13.5 MHz is far away from the maximum of the transmitted amplitude spectrum as shown in panel (d). This deviation from spectral maximum may cause a relatively small amplitude error Δ_A, but the error is significantly magnified by the large propagation factor F_α. This leads to incorrect attenuation results (hollow circles) as shown in panel (a). Instead, the corrected combination uses the model N11520 having smaller propagation factors in the frequency range of 6.5-13.5 MHz as shown in panel (b) and performs the FE simulations in an appropriate spectral range as shown in panel (d). The corrected results (solid triangles in panel (a)) agree very well with the theoretical curve, which is very accurate in the range of concern as explained in Sec. IV.D.1, while the incorrect results deviate substantially from both corrected and theoretical results. It is important to realize that the peak difference between the incorrect and corrected results, with the latter as reference, is as large as -54.78% occurring at the frequency of 6.5 MHz, see Fig. 12(a).

V. INCORPORATION OF STATISTICAL INFORMATION INTO THEORETICAL MODELS

The preceding FE method is capable of performing numerical experiments with fully-controlled conditions, and from the experiments effective media parameters can be ideally measured with errors and uncertainties being appropriately estimated. Thus, this method is well suited to evaluating theoretical models that are generally approximate due to the use of assumptions and simplifications. However, there remains one more challenge for accurate simulations, which is to determine the set of characteristics that are defined by a chosen FE model. Clearly the choices of

most parameters, such as, density, dimensions or crystal properties, are simply recorded. But the spatial characteristics of the grains are a product of the creation of the polycrystal domain, and these need to be measured from the FE model. This is a vital step for any comparative studies with analytical models, to ensure that these properties are represented properly in parallel in the FE and analytical models. In this third study we will investigate this challenge.

A. Statistical information required: two-point correlation function

The evaluation of a theoretical model requires its input statistical characteristics of the material system being measured from FE material models and its output being assessed against modelling results. For this reason, we aim to describe FE material models in a way that closely matches the need of theoretical models. As we have identified in our previous studies[18,19,21], the most significant element is the statistical description of the spatial variation of the material properties, namely the geometric two-point correlation (TPC) function, that is generally required for the advanced theoretical models.

The geometric TPC function, $w(r)$, is the probability of two points separated by a distance of r being in the same grain. A single-term exponential function, $w(r) = \exp(-r/a)$ (a is the correlation length), was traditionally used to describe polycrystals with untextured, equiaxed grains[5,8]. But this simplified function is substantially different from the TPC curve measured from a typical polycrystal model[18,32], and therefore it is essential to incorporate measured TPC data into theoretical models for more accurate evaluations.

To measure the TPC $w(r)$, previous procedures[18,32] drop a large number of random pairs of points, each pair being separated by a distance of r (see Fig. 13(a)), into a polycrystal model. Then they count the number of pairs whose two points occur in the same grain and compare this

number to the total number of pairs to obtain the probability $w(r)$. It is important to emphasize that a substantial number of tests, usually 1 million tests per discrete r, are required to obtain statistically converged TPC data.

To incorporate measured TPC data into a theoretical model, a mathematical function is constructed by best fitting the measured data. An optimal function of choice is the multi-term exponential function[18], $w(r) = \sum_i A_i \exp(-r/a_i)$, that has the advantage of delivering a simpler formulation for the theoretical model. The physical constraints on the coefficients A_i and a_i have been summarized in Van Pamel et al.[18] and the fitting can be achieved by using any nonlinear curve fitting algorithms.

In summary, the statistical information required for theoretical evaluations is the TPC function, which needs to be measured from FE models and fitted into a mathematical form.

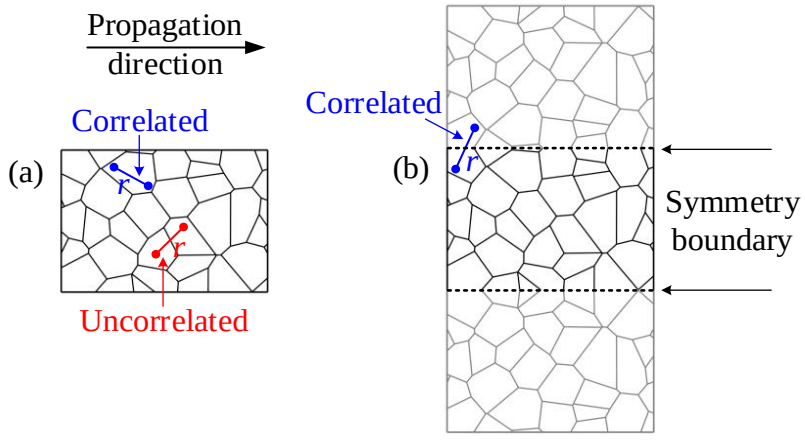


Fig. 13. (Color online) Illustration of (a) the measurement of two-point correlation function $w(r)$ and (b) the effect of symmetry boundary conditions. $w(r)$ is the probability that two points separated by a distance of r are correlated. Previous measurement procedures[18,32] only use internal points, which is shown in (a), to determine $w(r)$. In this case, two points are deemed correlated if they are in the same grain. As shown in (b), the use of symmetry boundary conditions

928 in the FE simulations leads to the mirroring of boundary grains. Due to this mirroring effect, two
929 points are also deemed correlated if they are in the same extended boundary grain.

930 B. Effect of symmetry boundary conditions

931 As shown in Fig. 13(a), previous procedures[18,32] to measure TPC data limit both points of a
932 random pair to the inside of a model, and thus consider only the statistical information within the
933 cuboid of the model. However, it is mentioned in Sec. II.C that we use symmetry boundary
934 conditions (SBCs) to emulate polycrystal media of infinite size in the transverse direction to that
935 of wave propagation. Such conditions mirror the boundary grains that are associated with SBCs,
936 which is demonstrated in Fig. 13(b), and these grains are therefore likely to be larger on average
937 than the grains located within the body of the model. And in the FE computations this results in
938 stronger scattering of propagating waves when they encounter enlarged boundary grains. Thus, it
939 might be desirable to consider this mirroring effect in the measurement of TPC data with a goal to
940 evaluate, by comparison with the FE results, which TPC is more appropriate for evaluating
941 theoretical results.

942 *1. Effect on two-point correlation function*

943 It can be inferred from the illustration in Fig. 13(b) that the statistical significance and impact of
944 the boundary grain mirroring increases as the proportion of boundary grains grows. Based on this
945 inference, now we evaluate the actual effect of SBCs on the TPC function. Achieving this
946 evaluation requires the grains associated with SBCs being parametrically described and the TPC
947 functions with consideration of SBCs being numerically measured.

948 To describe the grains associated with SBCs, we use three parameters: the number fraction NF and

volume fraction VF describing respectively the relative number and volume of boundary grains to all grains within the model, and the surface area to volume ratio SA:V representing the amount of symmetry boundary area per unit model volume. We calculate these parameters for the models given in Table I and provide the results in Table III with each of the coordinate axes being wave propagation direction. The table shows that for the provided models having significant numbers of grains, these three parameters are actually equivalent, with NF and VF being approximately equal to each other and being proportional to SA:V. It is important to realize that NF is slightly smaller than VF because the grains generated by the Voronoi tessellation do not have uniform volume, but rather boundary grains are to some degree larger than internal grains. Since these three parameters are equivalent, the following evaluation only uses the surface area to volume ratio SA:V to represent SBCs, because this parameter can be easily calculated without the knowledge of actual grains. And the studies reported below just consider, for the sake of clarity, the five cases in Table III with unique SA:V values: N115200-x, N11520-x, N11520-z, N16000-x, and N16000-z. Here the label of each case is composed of its model name and propagation direction.

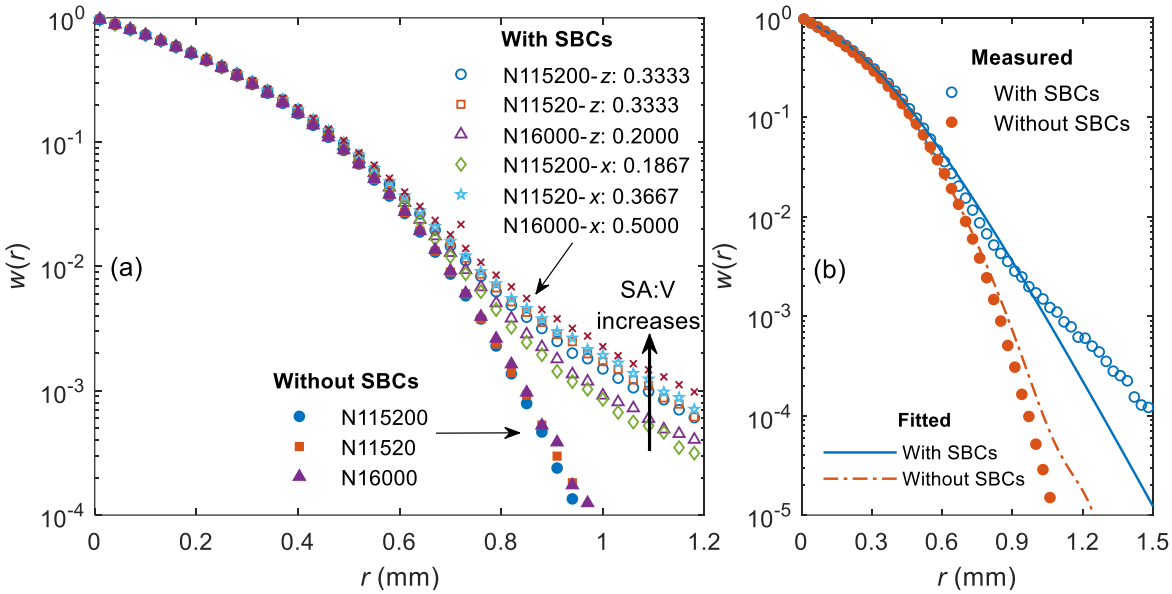
To measure the TPC functions with consideration of SBCs, we use a procedure that is mostly the same as the one summarized in Sec. V.A except for the two treatments adopted to consider SBCs. The first treatment is that for a pair of random points only one of them is confined within the model, while the other is completely random as long as their distance is r, meaning that the latter point can be outside of the model. Given a sufficiently large number of pairs, this allows the ergodicity to be satisfied, as the pairs can cover the entire space of infinite lateral extents that are prescribed by SBCs. The second treatment involves the counting of correlated pairs. As illustrated in Fig. 13(b), an extra situation of two points being correlated may occur when the second point is outside of the model. In this case, a pair is considered to be correlated if one point occurs in a symmetry

boundary grain and the other falls into its mirrored counterpart. By using this measurement procedure, the TPC data of the five cases given above are obtained and plotted in Fig. 14(a) as hollow points (the data points for the case N115200-z are also given in the figure for later use). To evaluate the influence of SBCs, the TPC statistics neglecting SBCs are also provided as solid points in the figure.

Table III. Parameters of the grains associated with symmetry boundary conditions. The parameters are given for three models, with information being provided in Table I, of waves propagating in three coordinate axes. NF and VF are the number and volume fractions, describing respectively the relative number and volume of symmetry boundary grains to all grains within a model. SA:V is the surface area to volume ratio, representing the amount of symmetry boundary area per unit model volume.

Model	x-direction propagation			y-direction propagation			z-direction propagation		
	NF	VF	SA:V	NF	VF	SA:V	NF	VF	SA:V
N115200	0.0860	0.0900	0.1867	0.0858	0.0896	0.1867	0.1482	0.1541	0.3333
N11520	0.1582	0.1714	0.3667	0.1614	0.1680	0.3667	0.1461	0.1555	0.3333
N16000	0.2244	0.2323	0.5000	0.2259	0.2329	0.5000	0.0908	0.0958	0.2000

A clear difference can be seen in Fig. 14(a) between the two sets of TPC points with and without consideration of SBCs, indicating that the mirroring of symmetry boundary grains has a substantial influence on TPC statistics. When SBCs are not considered, the data points of different models are almost overlapped. This suggests that the models adopted in the present work are essentially statistically equivalent and are of satisfactory statistical significance. When SBCs are taken into consideration, the measured statistics show evident discrepancies and these statistics are positively correlated with SA:V. The correlation is more pronounced at TPC tails, which reflects the increased grain sizes (or correlation lengths) caused by grain mirroring.



991

992 Fig. 14. (Color online) Two-point correlation data numerically measured from FE models (a) and
993 those related to actual FE simulations of this work (b). In (a), hollow points are collected with
994 consideration of symmetry boundary conditions (SBCs), while solid points ignore this SBCs effect.
995 The label of hollow points, N115200-*z*: 0.3333 for example, is started with model name (N115200),
996 followed by wave propagation direction (*z*), and ended with surface area to volume ratio SA:V
997 (0.3333). In (b), hollow points correspond to those of N11520-*z*: 0.3333 in (a), and solid points
998 are the averages of the solid ones in (a). These two sets of discrete data are fitted into mathematical
999 functions and are shown as lines. For better visualization, only every third point of measured data
1000 points are shown in the figure.

1001 The simulated waves travel in the *z*-direction, meaning that the consideration of SBCs involves
1002 only the cases associated with *z*-direction: N115200-*z*, N11520-*z* and N16000-*z*. It is shown in
1003 Fig. 14(a) that these three cases are quite close to each other, but N11520-*z* has the largest tail and
1004 thus the strongest SBCs effect. Therefore, this case is used in the following as an example for the
1005 consideration of SBCs, and it is further plotted in Fig. 14(b) as hollow circles. For the case of
1006 neglecting SBCs, the TPC data of the three models (Fig. 14(a)) are nearly identical. Thus, their

1007 average, provided in Fig. 14(b) as solid circles, is employed to describe the case of neglecting
1008 SBCs.

1009 It would be practically meaningful to reduce the impact of SBCs such that measuring TPC data
1010 can be performed in a simpler way by neglecting SBCs. This can be achieved by using smaller
1011 SA:Vs due to the positive correlation between TPC data and SA:V. It is shown in Table III that
1012 the way to get a smaller SA:V is through widening the lateral dimensions of polycrystal models,
1013 and in extreme cases the effect of SBCs can be negligible if the lateral dimensions are sufficiently
1014 wide. However, the models adopted in the present work are already very big and increasing their
1015 lateral dimensions will lead to added challenges to our computation resources. In addition, an
1016 alternative possibility of minimizing SBCs effect is to reduce the average size of the symmetry
1017 boundary grains such that the mirrored grains would have similar sizes to internal grains. It is
1018 practically difficult to generate grains with such a distribution but implementing a method for this
1019 aim would be very useful.

1020 *2. Effect on attenuation and phase velocity*

1021 Having demonstrated in the preceding examination that SBCs have a significant effect on TPC
1022 functions, it is now essential to identify if SBCs would equally affect effective media parameters
1023 in terms of attenuation coefficient and phase velocity. For this purpose, we input the TPC functions,
1024 with and without consideration of SBCs, into one of the advanced theoretical models, the second-
1025 order approximation (SOA)[18], to calculate the parameters. The degrees of agreement between
1026 the resulting parameters and FE results are then estimated to assess the improvement brought in
1027 by the consideration of SBCs.

1028 Incorporating TPC functions into the SOA model requires the two sets of data in Fig. 14(b) to be

fitted to mathematical forms. The process discussed in Sec. V.A is used here and a multi-term exponential function is chosen as the fitting function. The fitting is performed in a least squares sense, and the number of exponential terms is selected as eight because the fitting can be unstable if a larger number is used. The coefficients of the fitted functions are listed in Table IV. The functions are further plotted in Fig. 14(b), showing reasonably good fittings.

Table IV. Coefficients of mathematically fitted two-point correlation functions. A_i and a_i are coefficients of the i-th term of the mathematically fitted function $w(r) = \sum_i A_i \exp(-r/a_i)$.

Terms	Without SBCs		With SBCs	
	A_i	a_i	A_i	a_i
1	-2922.66	0.115726	-129.485	0.1280002
2	-10.6181	0.172221	-388.413	0.1279995
3	3914.370	0.110790	797.091	0.1517330
4	-3305.68	0.103201	-1372.040	0.1898924
5	696.919	0.0910265	1982.690	0.1867733
6	54.3582	0.152263	694.300	0.1242404
7	-42.4732	0.0723540	-469.525	0.1279995
8	1616.78	0.110790	-1113.610	0.1709402

Substituting the two fitted functions into the SOA model and solving the equation results in the theoretical solutions to attenuation and phase velocity. Here we use Inconel, the properties of which are given in Table II, as the material input to calculate theoretical solutions. The resulting attenuation and velocity curves are plotted in Fig. 15(a) and (b), respectively. In the figure, the corresponding FEM results are also provided as baseline data to evaluate the approximations of these solutions.

It is shown in Fig. 15(a) and (b) that the overall agreement between the theoretical and FEM results is very good, no matter whether SBCs are considered in the TPC functions or not. However, there

1044 are clear differences between the theoretical results, which demonstrates that the SBCs effect is
1045 actually prominent. In most frequency regions, the curves with consideration of SBCs agree better
1046 with FEM points, conveying an essential message that the FEM results are influenced by the
1047 doubling of grain size at symmetry boundaries. It is also important to notice that the theoretical
1048 and FEM results are not perfectly matched even when boundary grains are considered. This is
1049 because in the FEM results the SBCs affect scattering only at boundaries, while in the theoretical
1050 model the effect is not reproduced exactly as the TPC function assumes random, homogeneous
1051 distribution of those grains.

1052 There is no doubt that the TPC function with SBCs should be selected for our material systems
1053 when evaluating the theoretical model. To quantify the improvement of theoretical prediction
1054 brought in by the consideration of SBCs, we calculate the relative differences of theoretical curves
1055 to the FEM points and plot them in Fig. 15(c) and (d). The agreement is clearly better at all
1056 frequencies for the TPC function with SBCs.

1057 The conclusion of this investigation is that it is best to consider the SBCs effect in the TPC function.
1058 In practice, however, it is always desirable to reduce the effect of the boundaries to a negligible
1059 level by making a model as wide as possible. It is important to do so, because one of the key
1060 interests of FE modelling at the moment is to check the significance of assumptions in analytical
1061 models, and thus there is a strong motivation to eliminate this TPC source of differences from the
1062 modelling.

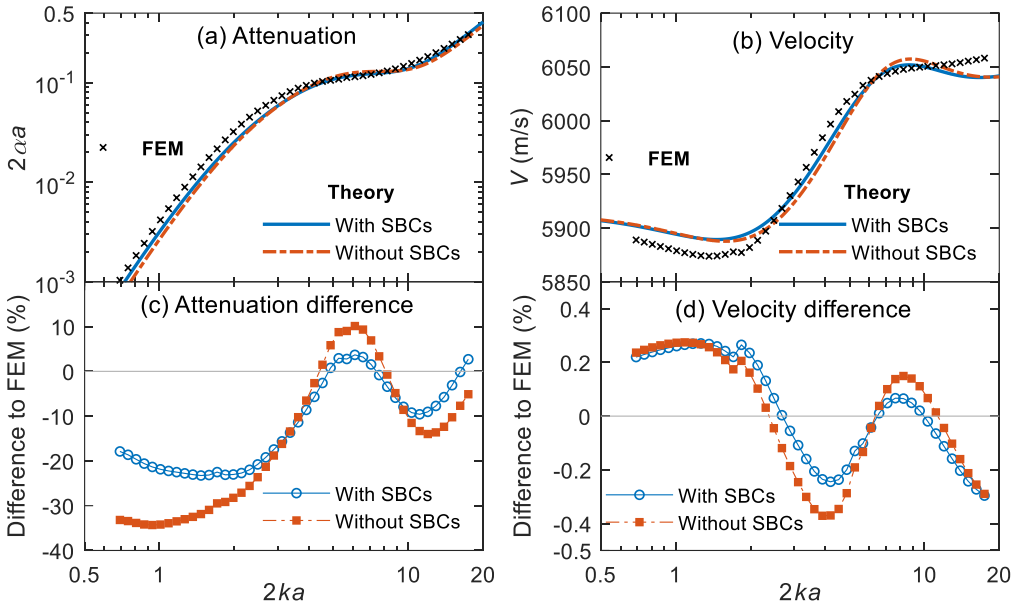


Fig. 15. (Color online) Comparison of theoretically predicted effective media parameters with FEM results for Inconel: (a) attenuation, (b) phase velocity, (c) relative difference of attenuation, and (d) relative difference of phase velocity. In (a) and (b), lines represent the theoretical solutions of the SOA model which uses the two-point correlation functions with (solid lines) and without (dash-dotted lines) consideration of symmetry boundary conditions (SBCs). Crosses denote the FEM results obtained from the models N115200, N11520 and N16000. Each model uses 15 realizations to obtain the averaged results shown in the figure. For better visualization only every ten points of FEM data are shown here. In (c) and (d), the relative differences are computed by subtracting FEM results from theoretical predictions, and then dividing by FE results.

VI. SUMMARY AND CONCLUSION

This work presents a thorough study of the finite element (FE) method for the propagation and scattering of elastic waves in polycrystals. Specifically, this work addresses the following three topics that have not been covered by the modelling studies so far but are essential to future FE simulations.

The determination of effective media parameters, namely attenuation and phase velocity, is first discussed. These parameters describe the amplitude and phase changes of a plane wave as it travels through a polycrystalline medium. It is demonstrated that the travelling wave essentially does not have a planar wavefront, which is caused by random scattering. However, it is demonstrated that the coherent part, belonging to the plane wave, can be conveniently calculated as the spatial average of the wavefront. From a set of coherent waves, attenuation and phase velocity can be determined in two ways. The through-transmission approach uses the coherent waves measured on two external surfaces: the transmitting surface and its opposite receiving surface. In addition to the two waves used in the through-transmission method, the fitting approach also utilizes extra coherent waves collected inside an FE model. These two approaches are found to be practically equivalent and can thus be used interchangeably. The through-transmission method might be preferable in actual simulations due to its ease of wave collection and calculation.

The estimation and suppression of the errors and uncertainties of effective media parameters are then attempted in this study. It is found that two factors can cause errors and uncertainties: numerical approximations and statistical considerations. Numerical approximations only cause errors, while statistical considerations involve both errors and uncertainties. For numerical errors, both attenuation and velocity errors can be suppressed by the use of a larger spatial sampling number S (thus a finer mesh size h) if computational capability allows. In addition to this, numerical attenuation and velocity errors can also be reduced in different ways: 1) Numerical attenuation error can be suppressed by using an appropriate spectrum range that is in close proximity to its maximum, or by limiting attenuation αd to a certain range in the vicinity of 1 Neper. 2) Numerical velocity error can be controlled by using a large Courant number C that is close to unity, and can also be corrected by utilizing the analytically predicted error from Eq. (7).

For statistical errors and uncertainties, the suppression approaches developed for numerical errors also ensure that they can be satisfactorily controlled to a certain extent. The only requirement is that a sufficiently large number N of realizations has to be used to obtain a reasonably small statistical error and a fairly converged statistical uncertainty.

The incorporation of FE model information into theoretical models is finally discussed. It is indicated that the two-point correlation (TPC) function is the statistic required to put into theories. The symmetry boundary conditions (SBCs), employed to emulate infinitely wide media that can hold plane waves, have a considerable effect on the TPC function and on the theoretically predicted attenuation and velocity. Thus, this SBCs effect needs to be considered in the TPC function for a more accurate incorporation of statistical information.

The FE method discussed in this work focuses on the specific case of plane longitudinal waves travelling in untextured polycrystals with equiaxed grains. However, it is expected that the principle established in this work may be extended reliably to more general cases, for example to elongated grains and preferred crystallographic texture materials.

ACKNOWLEDGEMENTS

The authors acknowledge Dr. A. Van Pamel for his valuable suggestions on studying symmetry boundary conditions. M.H. was supported by the Chinese Scholarship Council and the Beijing Institute of Aeronautical Materials. P.H. was funded by the UK Engineering and Physical Sciences Research Council (EPSRC) fellowship EP/M020207/1. M.J.S.L. was partially sponsored by the EPSRC. G.S. and S.I.R. were partially supported by the AFRL (USA) under the prime contract FA8650-10-D-5210.

REFERENCES

[1]R. B. Thompson, F. J. Margetan, P. Haldipur, L. Yu, A. Li, P. D. Panetta, and H. Wasan, "Scattering of elastic waves in simple and complex polycrystals," Wave Motion **45**, 655–674 (2008).

[2]J. Li and S. I. Rokhlin, "Propagation and scattering of ultrasonic waves in polycrystals with arbitrary crystallite and macroscopic texture symmetries," Wave Motion **58**, 145–164 (2015).

[3]P. Palanichamy, A. Joseph, T. Jayakumar, and B. Raj, "Ultrasonic velocity measurements for estimation of grain size in austenitic stainless steel," NDT E Int. **28**, 179–185 (1995).

[4]E. P. Papadakis, "Ultrasonic attenuation caused by scattering in polycrystalline media," in *Physical Acoustics IV: Part B*, edited by W. P. Mason (Academic Press, New York and London, 1968), pp. 269–328.

[5]F. E. Stanke and G. S. Kino, "A unified theory for elastic wave propagation in polycrystalline materials," J. Acoust. Soc. Am. **75**, 665–681 (1984).

[6]F. C. Karal and J. B. Keller, "Elastic, electromagnetic, and other waves in a random medium," J. Math. Phys. **5**, 537–547 (1964).

[7]J. B. Keller, "Stochastic equations and wave propagation in random media," in *Proceedings of Symposia in Applied Mathematics*, Vol. XVI, edited by R. Bellman (American Mathematical Society, Providence, RI, 1964), pp. 145–177.

[8]R. L. Weaver, "Diffusivity of ultrasound in polycrystals," J. Mech. Phys. Solids **38**, 55–86 (1990).

[9]U. Frisch, "Wave propagation in random media.," in *Probabilistic Methods in Applied*

Mathematics, edited by A. Bharucha-Reid (Academic Press, New York, 1968), pp. 75–198.

[10]J. A. Turner, "Elastic wave propagation and scattering in heterogeneous anisotropic media: Textured polycrystalline materials," J. Acoust. Soc. Am. **106**, 541–552 (1999).

[11]L. Yang, O. I. Lobkis, and S. I. Rokhlin, "Shape effect of elongated grains on ultrasonic attenuation in polycrystalline materials," Ultrasonics **51**, 697–708 (2011).

[12]A. Bhattacharjee, A. L. Pilchak, O. I. Lobkis, J. W. Foltz, S. I. Rokhlin, and J. C. Williams, "Correlating ultrasonic attenuation and microtexture in a near-alpha titanium alloy," Metall. Mater. Trans. A **42**, 2358–2372 (2011).

[13]M. Calvet and L. Margerin, "Velocity and attenuation of scalar and elastic waves in random media: A spectral function approach," J. Acoust. Soc. Am. **131**, 1843–1862 (2012).

[14]L. Yang, J. Li, O. I. Lobkis, and S. I. Rokhlin, "Ultrasonic propagation and scattering in duplex microstructures with application to titanium alloys," J. Nondestruct. Eval. **31**, 270–283 (2012).

[15]L. Yang, J. Li, and S. I. Rokhlin, "Ultrasonic scattering in polycrystals with orientation clusters of orthorhombic crystallites," Wave Motion **50**, 1283–1302 (2013).

[16]C. M. Kube, "Iterative solution to bulk wave propagation in polycrystalline materials," J. Acoust. Soc. Am. **141**, 1804–1811 (2017).

[17]M. Calvet and L. Margerin, "Impact of grain shape on seismic attenuation and phase velocity in cubic polycrystalline materials," Wave Motion **65**, 29–43 (2016).

[18]A. Van Pamel, G. Sha, M. J. S. Lowe, and S. I. Rokhlin, "Numerical and analytic modelling of elastodynamic scattering within polycrystalline materials," J. Acoust. Soc. Am. **143**, 2394–2408

(2018).

[19]G. Sha, M. Huang, M. J. S. Lowe, and S. I. Rokhlin, "Attenuation and velocity of elastic waves in polycrystals with generally anisotropic grains: analytic and numerical modelling," J. Acoust. Soc. Am. **147**, 2422–2465 (2020).

[20]S. I. Rokhlin, J. Li, and G. Sha, "Far-field scattering model for wave propagation in random media," J. Acoust. Soc. Am. **137**, 2655–2669 (2015).

[21]A. Van Pamel, G. Sha, S. I. Rokhlin, and M. J. S. Lowe, "Finite-element modelling of elastic wave propagation and scattering within heterogeneous media," Proc. R. Soc. A Math. Phys. Eng. Sci. **473**, 1–21 (2017).

[22]M. Frehner, S. M. Schmalholz, E. H. Saenger, and H. Steeb, "Comparison of finite difference and finite element methods for simulating two-dimensional scattering of elastic waves," Phys. Earth Planet. Inter. **171**, 112–121 (2008).

[23]G. Ghoshal and J. A. Turner, "Numerical model of longitudinal wave scattering in polycrystals," IEEE Trans. Ultrason. Ferroelectr. Freq. Control **56**, 1419–1428 (2009).

[24]S. Shahjahan, F. Rupin, A. Aubry, B. Chassignole, T. Fouquet, and A. Derode, "Comparison between experimental and 2-D numerical studies of multiple scattering in Inconel600® by means of array probes," Ultrasonics **54**, 358–367 (2014).

[25]P.-E. Lhuillier, B. Chassignole, M. Oudaa, S. O. Kerhervé, F. Rupin, and T. Fouquet, "Investigation of the ultrasonic attenuation in anisotropic weld materials with finite element modeling and grain-scale material description," Ultrasonics **78**, 40–50 (2017).

[26]S. Shivaprasad, C. V. Krishnamurthy, and K. Balasubramaniam, "Modeling and simulation of

ultrasonic beam skewing in polycrystalline materials," Int. J. Adv. Eng. Sci. Appl. Math. **10**, 70–78 (2018).

[27]X. Bai, B. Tie, J.-H. Schmitt, and D. Aubry, "Finite element modeling of grain size effects on the ultrasonic microstructural noise backscattering in polycrystalline materials," Ultrasonics **87**, 182–202 (2018).

[28]A. Boström and A. Ruda, "Ultrasonic attenuation in polycrystalline materials in 2D," J. Nondestruct. Eval. **38**, 47:1–6 (2019).

[29]A. Van Pamel, P. B. Nagy, and M. J. S. Lowe, "On the dimensionality of elastic wave scattering within heterogeneous media," J. Acoust. Soc. Am. **140**, 4360–4366 (2016).

[30]P. Huthwaite, "Accelerated finite element elastodynamic simulations using the GPU," J. Comput. Phys. **257**, 687–707 (2014).

[31]A. Van Pamel, C. R. Brett, P. Huthwaite, and M. J. S. Lowe, "Finite element modelling of elastic wave scattering within a polycrystalline material in two and three dimensions," J. Acoust. Soc. Am. **138**, 2326–2336 (2015).

[32]M. Ryzy, T. Grabec, P. Sedlák, and I. A. Veres, "Influence of grain morphology on ultrasonic wave attenuation in polycrystalline media," J. Acoust. Soc. Am. **143**, 219–229 (2018).

[33]B. Yue and M. N. Guddati, "Dispersion-reducing finite elements for transient acoustics," J. Acoust. Soc. Am. **118**, 2132–2141 (2005).

[34]M. B. Drozdz, "Efficient finite element modelling of ultrasound waves in elastic media," Ph.D. thesis, Imperial College London, London, 2008.

[35]R. Quey, P. R. Dawson, and F. Barbe, "Large-scale 3D random polycrystals for the finite element method: Generation, meshing and remeshing," Comput. Methods Appl. Mech. Eng. **200**, 1729–1745 (2011).

[36]M. A. Groeber and M. A. Jackson, "DREAM.3D: A digital representation environment for the analysis of microstructure in 3D," Integr. Mater. Manuf. Innov. **3**, 56–72 (2014).

[37]R. D. Cook, D. S. Malkus, M. E. Plesha, and R. J. Witt, "Concepts and applications of finite element analysis," (John Wiley & Sons, Inc., New York, NY, 2002).

[38]P. Langer, M. Maeder, C. Guist, M. Krause, and S. Marburg, "More Than Six Elements per Wavelength: The Practical Use of Structural Finite Element Models and Their Accuracy in Comparison with Experimental Results," J. Comput. Acoust. **25**, 1–23 (2017).

[39]J. S. Zhang, M. Hao, Z. Ren, and B. Chen, "The extreme acoustic anisotropy and fast sound velocities of cubic high-pressure ice polymorphs at Mbar pressure," Appl. Phys. Lett. **114**, 191903 (2019).

[40]A. Ishimaru, "Wave propagation and scattering in random media and rough surfaces," Proc. IEEE **79**, 1359–1366 (1991).

[41]K.-J. Bathe, "Finite element procedures in engineering analysis," (Prentice-Hall, New Jersey, USA, 1982).

[42]R. Mullen and T. Belytschko, "Dispersion analysis of finite element semidiscretizations of the two-dimensional wave equation," Int. J. Numer. Methods Eng. **18**, 11–29 (1982).

[43]K. J. Marfurt, "Accuracy of finite-difference and finite-element modeling of the scalar and elastic wave equations," Geophysics **49**, 533–549 (1984).

[44]M. A. Dokainish and K. Subbaraj, "A survey of direct time-integration methods in computational structural dynamics—I. Explicit methods," Comput. Struct. **32**, 1371–1386 (1989).

[45]I. Harari, K. Grosh, T. J. R. Hughes, M. Malhotra, P. M. Pinsky, J. R. Stewart, and L. L. Thompson, "Recent developments in finite element methods for structural acoustics," Arch. Comput. Methods Eng. **3**, 131–309 (1996).

[46]A. Deraemaeker, I. Babuška, and P. Bouillard, "Dispersion and pollution of the FEM solution for the Helmholtz equation in one, two and three dimensions," Int. J. Numer. Methods Eng. **46**, 471–499 (1999).

[47]H. P. Cherukuri, "Dispersion analysis of numerical approximations to plane wave motions in an isotropic elastic solid," Comput. Mech. **25**, 317–328 (2000).

[48]L. L. Thompson, "A review of finite-element methods for time-harmonic acoustics," J. Acoust. Soc. Am. **119**, 1315–1330 (2006).

[49]R. Kolman, J. Plešek, J. Červ, M. Okrouhlík, and P. Pařík, "Temporal-spatial dispersion and stability analysis of finite element method in explicit elastodynamics," Int. J. Numer. Methods Eng. **106**, 113–128 (2016).

[50]S. Geevers, W. A. Mulder, and J. J. W. van der Vegt, "Dispersion properties of explicit finite element methods for wave propagation modelling on tetrahedral meshes," J. Sci. Comput. **77**, 372–396 (2018).

[51]A. N. Kalashnikov and R. E. Challis, "Errors and uncertainties in the measurement of ultrasonic wave attenuation and phase velocity," IEEE Trans. Ultrason. Ferroelectr. Freq. Control **52**, 1754–1768 (2005).

1245